Original article

Targeted delivery of rosuvastatin enhances treatment of hyperhomocysteinemia-induced atherosclerosis using macrophage membrane-coated nanoparticles

Dayue Liu [a, b, c, 1], Anning Yang [a, d, e, 1], Yulin Li [a, b, c], Zhenxian Li [f], Peidong You [a, b, c], Hongwen Zhang [a, b, c], Shangkun Quan [a, b, c], Yue Sun [b, d, e], Yaling Zeng [a, b, c], Shengchao Ma [a, b, c], Jiantuan Xiong [b, c], Yinju Hao [b, d], Guizhong Li [a, b, c], Bin Liu [a, e, g, ***], Huiping Zhang [d, e, g, **], Yideng Jiang [a, b, c, *]

[a] Department of Pathophysiology, School of Basic Medical Sciences, Ningxia Medical University, Yinchuan, 750004, China
[b] NHC Key Laboratory of Metabolic Cardiovascular Diseases Research, Ningxia Medical University, Yinchuan, 750004, China
[c] Ningxia Key Laboratory of Vascular Injury and Repair Research, Ningxia Medical University, Yinchuan, 750004, China
[d] General Hospital of Ningxia Medical University, Yinchuan, 750004, China
[e] College of Biology, Hunan University, Changsha, 410082, China
[f] Hunan University of Chinese Medicine, First Clinical College of Traditional Chinese Medicine, Changsha, 410007, China
[g] Hunan Provincial Maternal and Child Health Care Hospital, Changsha, 410000, China

ARTICLE INFO

ABSTRACT

Rosuvastatin (RVS) is an excellent drug with anti-inflammatory and lipid-lowering properties in the academic and medical fields. However, this drug faces a series of challenges when used to treat atherosclerosis caused by hyperhomocysteinemia (HHcy), including high oral dosage, poor targeting, and long-term toxic side effects. In this study, we applied nanotechnology to construct a biomimetic nano-delivery system, macrophage membrane (Møm)-coated RVS-loaded Prussian blue (PB) nanoparticles (MPR NPs), for improving the bioavailability and targeting capacity of RVS, specifically to the plaque lesions associated with HHcy-induced atherosclerosis. *In vitro* assays demonstrated that MPR NPs effectively inhibited the Toll-like receptor 4 (TLR4)/hypoxia-inducible factor-1α (HIF-1α)/nucleotide-binding and oligomerization domain (NOD)-like receptor thermal protein domain associated protein 3 (NLRP3) signaling pathways, reducing pyroptosis and inflammatory response in macrophages. Additionally, MPR NPs reversed the abnormal distribution of adenosine triphosphate (ATP)-binding cassette transporter A1 (ABCA1)/ATP binding cassette transporter G1 (ABCA1)/ATP binding cassette transporter G1 (ABCG1) caused by HIF-1α, promoting cholesterol efflux and reducing lipid deposition. *In vivo* studies using apolipoprotein E knockout ($ApoE^{-/-}$) mice confirmed the strong efficacy of MPR NPs in treating atherosclerosis with favorable biosecurity, and the mechanism behind this efficacy is believed to involve the regulation of serum metabolism and the remodeling of gut microbes. These findings suggest that the synthesis of MPR NPs provides a promising nanosystem for the targeted therapy of HHcy-induced atherosclerosis.

1. Introduction

Hyperhomocysteinemia (HHcy) is recognized as an independent risk factor for atherosclerosis [1]. Increased homocysteine (Hcy) levels promote the formation of macrophage-derived foam cells and enhance inflammatory responses during plaque development [2]. While folic acid and vitamin B12 are commonly used for HHcy treatment, they are ineffective in reducing lipid deposition and inflammation in blood vessels. Rosuvastatin (RVS), a first-

* Corresponding author. Department of Pathophysiology, School of Basic Medical Sciences, Ningxia Medical University, Yinchuan, 750004, China.
** Corresponding author. Hunan Provincial Maternal and Child Health Care Hospital, Changsha, 410000, China.
*** Corresponding author. College of Biology, Hunan University, Changsha, 410082, China.
E-mail addresses: jydeng@nxmu.edu.cn (Y. Jiang), zhp19760820@163.com (H. Zhang), binliu2001@hotmail.com (B. Liu).
[1] Both authors contributed equally to this work.

class drug known for its anti-inflammatory and lipid-lowering properties, has shown promise in atherosclerosis therapy. However, its limited bioavailability, poor targeting, and potential liver and kidney injury restrict its widespread use [3]. Consequently, the development of nanocarriers for improved drug delivery has gained attention in atherosclerosis prevention and treatment [4]. Prussian blue (PB) nanoparticles (NPs), with their biocompatibility and unique metal-organic framework structure, have emerged as potential therapeutic agents and carriers [5]. Moreover, PB NPs possess catalase activity, thereby exhibiting anti-inflammatory effects [6]. Nonetheless, their non-specific targeting of plaques may lead to systemic side effects. Interestingly, macrophage membrane (Møm) camouflage has been reported to enhance NPs accumulation at specific lesion sites by evading immune cell phagocytosis and clearance due to natural chemotaxis towards inflammation [7].

Hcy, through redox reactions, generates reactive oxygen species (ROS) and plays a crucial role in activating the nucleotide-binding and oligomerization domain (NOD)-like receptor thermal protein domain associated protein 3 (NLRP3) [8], leading to pyroptosis mediated inflammatory response. In 2015, Shao and co-workers [9] first elucidated the molecular mechanism of cell pyroptosis, characterized by continuous cell swelling, dissolution of the cell membrane, and the release of inflammatory factors [10]. This type of cell death is initiated by NLRP3, which binds to apoptosis-associated speck-like protein (ASC) to form an inflammasome with pro-caspase-1, ultimately activating caspase-1. Next, the N-terminal fragment of gasdermin D (GSDMD) with caspase-1 cleavage can penetrate the membrane to release mature interleukin (IL)-1β and IL-18, thereby exacerbating the inflammatory response. Toll-like receptor 4 (TLR4), a critical regulator of inflammation, can be activated by Hcy [11]. Activation of TLR4 further induces NLRP3 inflammasome-mediated pyroptosis in macrophages [12]. Moreover, Hcy induces mitochondrial oxidative damage and the release of ROS, which activates hypoxia-inducible factor-1α (HIF-1α). HIF-1α is involved in the regulation of NLRP3 inflammasome-mediated pyroptosis [13]. Based on these findings, we propose that Møm-coated RVS-loaded PB (MPR) NPs can effectively treat Hcy-induced atherosclerosis by inhibiting macrophage pyroptosis.

There is a growing body of evidence supporting the use of metabolomics as an effective approach for discovering new biomarkers and understanding the underlying pathogenic mechanisms of atherosclerosis. Metabolic analysis can uncover how metabolites interact with specific inflammasome proteins and mediators of cell pyroptosis during atherosclerosis development [14]. Additionally, studies have shown that apolipoprotein E knockout ($ApoE^{-/-}$) mice fed a high methionine diet (HMD) not only exhibit elevated Hcy levels but also experience alterations in the composition of gut microbiota. This dietary intervention reduces the abundance of beneficial bacteria, such as *Bacteroidetes* and *Verrucomicrobia*, while increasing the abundance of harmful bacteria, such as *Firmicutes* [15]. Hcy can also increase intestinal permeability, facilitating the enrichment of harmful microorganisms near atherosclerotic plaques during circulation, thereby triggering oxidative stress and an inflammatory response [16]. Notably, gut microbes have emerged as potential therapeutic targets for treating atherosclerosis-associated cardiovascular diseases [17]. As such, regulating metabolites and modulating gut microbiota hold promises for HHcy-induced atherosclerosis therapy.

In this study, we developed a novel approach for HHcy-induced atherosclerosis therapy using MPR NPs. This nanodrug system improves immune evasion in the bloodstream and enhances targeting capability to plaque sites. We validated the therapeutic efficacy of this system in both Hcy-induced macrophages and HMD-fed $ApoE^{-/-}$ mice, providing evidence for its effectiveness in treating atherosclerosis. Additionally, we unraveled the underlying

molecular mechanisms by which these NPs inhibit Hcy-induced macrophage pyroptosis, highlighting the regulation of the TLR4/HIF-1α/NLRP3 signaling pathways. To assess the broader impact of these NPs, we employed metabonomic analysis and 16S ribosomal DNA (rDNA) technology to explore their effects on metabolites and gut microbes in $ApoE^{-/-}$ mice (Scheme 1).

2. Materials and methods

2.1. Materials

RVS was obtained from Solarbio Science and Technology Co., Ltd. (IR0150; Beijing, China), while $K_3[Fe(CN)_6] \cdot 3H_2O$ was purchased from Aladdin Biochemical Technology Co., Ltd. (Shanghai, China). Poly(*N*-vinylpyrrolidone) (PVP) was sourced from Zhanyun Chemical Co., Ltd. (Shanghai, China). Hcy (H4628) was acquired from Sigma-Aldrich (Saint Louis, MO, USA). Rhodamine B (B20789) was supplied by Yuanye Bio-Technology Co., Ltd. (Shanghai, China), and indocyanine green (ICG) was acquired from Acros-Organics (Morris Plains, NJ, USA). Lipofectamine 2000 was purchased from Life Technologies (Gaithersburg, MD, USA).

2.2. Preparation of NPs

2.2.1. Preparation of PB NPs

A mixture of 66 mg of $K_3[Fe(CN)_6] \cdot 3H_2O$ and 1.5 g of PVP dissolved in 20 mL of 0.01 M HCl was added to an 80 °C oil bath and stirred for 20 h. The resulting material was collected by centrifugation at 13,000 r/min for 30 min. The solid PB NPs were then resuspended in ddH₂O and subjected to centrifugation for four cycles to obtain solid PB NPs. To prepare PB NPs from the solid form, 10 mg of solid PB NPs and 50 mg of PVP were dissolved in 10 mL of 1 M HCl. The resulting solution was then added to the reaction mixture and stirred for 4 h. The precipitates were obtained through centrifugation and washed four times. Finally, the precipitate was freeze-dried overnight to obtain mesoporous PB NPs.

2.2.2. Preparation of Møm

To extract Møm, 10 μL of phenylmethanesulfonyl fluoride (PMSF) and 1 mL of membrane extraction reagent were mixed with 2.0×10^7 RAW264.7 cells. After incubation for 40 min, the cell lysates were sonicated using an ultrasonic probe and subjected to four cycles of freeze-thawing under liquid nitrogen and 37 °C conditions. Subsequently, the supernatant was obtained by centrifugation at 1,000 r/min for 5 min. The final supernatant was further centrifuged at 13,000 r/min for 30 min to isolate the Møm.

2.2.3. Preparation of MPR NPs

To prepare the MPR NPs, RVS (final concentration at 500 μg/mL) and PB NPs (final concentration at 500 μg/mL) were stirred together at 4 °C for 12 h. The unloaded RVS was subsequently removed by centrifugation. The Møm and PB NPs were then mixed at a membrane protein weight ratio of 4:1, respectively. The resulting mixture underwent ultrasound treatment for 10 min and was subsequently extruded through a 0.22-μm polyethersulfone membrane to obtain the MPR NPs.

2.3. Characterization of MPR NPs

2.3.1. Characterization of NPs

The morphology of the NPs was examined using a transmission electron microscope (TEM; JEM-2100 Plus, JEOL, Tokyo, Japan). The ultraviolet-visible (UV-vis) absorption spectrum was employed to evaluate the drug encapsulation efficiency (EE) and drug loading efficiency (LE) at various ratios. The size and zeta potential of the
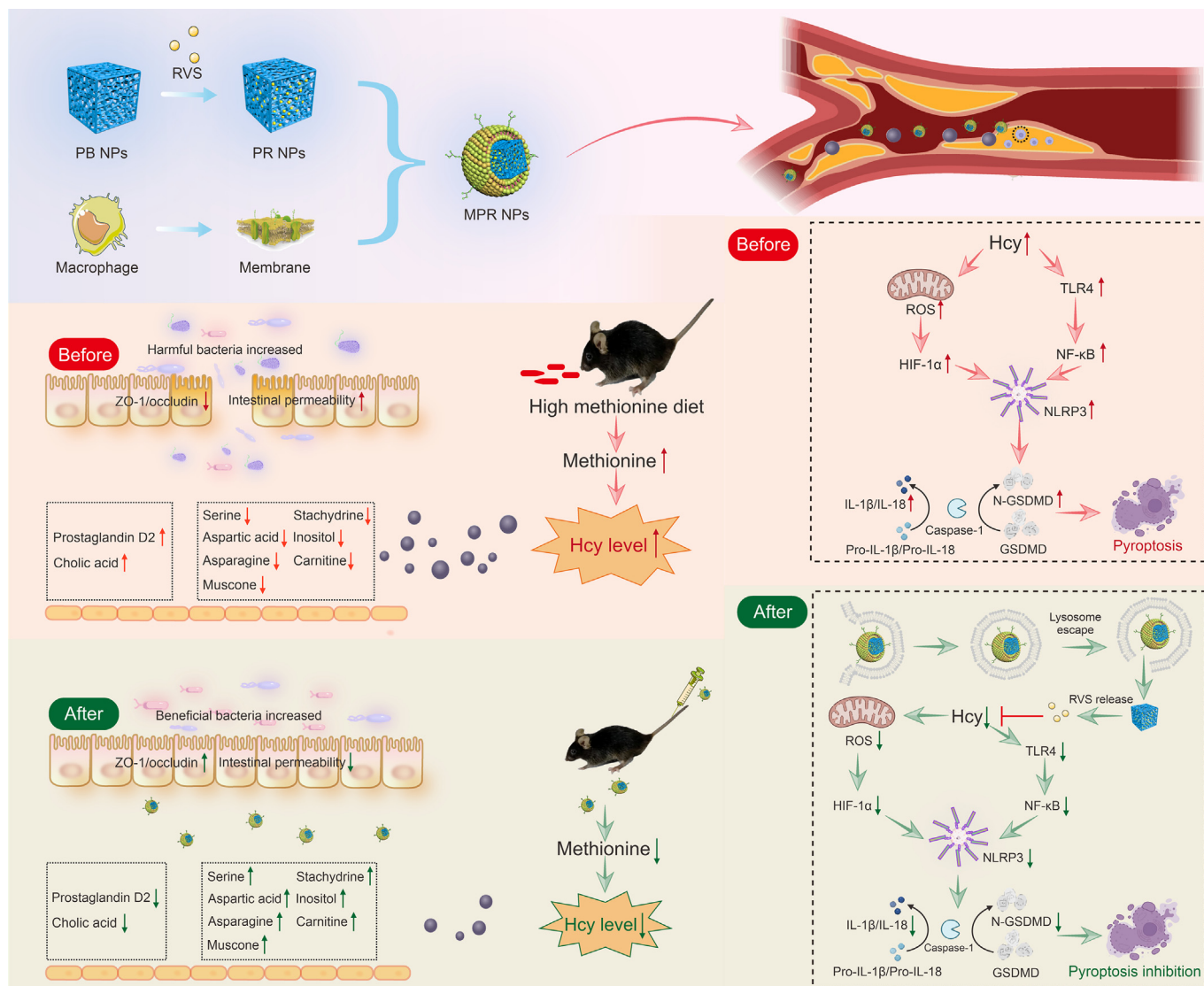
Scheme 1. Construction a biomimetic nano-drug treat homocysteine (Hcy)-induced atherosclerosis by inhibiting macrophage pyroptosis. Additionally, this nano-drug improves the dysbiosis of gut microbes while reducing the inflammatory response and blood Hcy levels. PB: Prussian blue; NPs: nanoparticles; RVS: rosuvastatin; PR: RVS-loaded PB; MPR: macrophage membrane-coated PR; ZO-1: zonula occludens-1; ROS: reactive oxygen species; HIF-1α: hypoxia-inducible factor-1α; TLR4: Toll-like receptor 4; NF-κB: nuclear factor kappaB; NLRP3: oligomerization domain (NOD)-like receptor thermal protein domain associated protein 3; IL: interleukin; GSDMD: gasdermin D; N-GSDMD: N-terminal GSDMD.

NPs were measured using dynamic light scattering (DLS; Nano ZS90 Zeta sizer, Malvern Instruments Ltd., Westborough, MA, USA). Furthermore, Fourier transform infrared spectroscopy (FT-IR) was utilized to identify the chemical bonds present in the NPs.

2.3.2. Characterization of Møm

Membrane proteins were extracted from Møm and MPR NPs using a membrane protein extraction kit following the provided instructions. The extracted membrane proteins were then subjected to analysis using sodium dodecyl sulfate-polyacrylamide gel electrophoresis (SDS-PAGE) gels, and their profiles were assessed by Coomassie brilliant blue staining. Western blotting was performed to detect the presence of the Møm protein-specific marker, a cluster of differentiation 11b (CD11b).

Møm were labeled with 1,1-dioctadecyl-3,3,3,3-tetramethylindocarbocyanine perchlorate (DiL) dye (green), while PB NPs were labeled with 1,1-dioctadecyl-3,3,3,3-tetramethylindodicarbocyanine perchlorate (DiD) dye (red). The

two samples were subsequently mixed and incubated at 37 °C for 1 h. Visualization of the samples was then carried out using confocal laser scanning microscopy (CLSM) with an Olympus FV1200 (Tokyo, Japan) instrument. The colocalization of the red and green signals were assessed to determine the accuracy of PB NP encapsulation within the membranes.

2.4. Cell culture

The mouse macrophage cell (RAW264.7), human umbilical vein endothelial cell (HUVEC), vascular smooth muscle cell (VSMC), human liver cell (HL7702), and human colorectal adenocarcinoma cell (Caco-2) were obtained from the Cell Bank of the Chinese Academy of Sciences (Shanghai, China). These cells were cultured in Dulbecco's modified Eagle medium (DMEM; Gibco, New York City, NY, USA) supplemented with 10% fetal bovine serum (FBS; Gibco) and 1% streptomycin (Invitrogen, Carlsbad, CA, USA) at 37 °C in a 5% CO_2 incubator.

For cell transfection, small interfering RNAs (siRNA) against TLR4 (si-TLR4) and negative control siRNA (si-NC) were obtained from GenePharma (Shanghai, China). To prepare the transfection mixture, solution A, consisting of 250 μL of DMEM and 5 μL of Lipofectamine 2000 (11668030; Invitrogen), was kept at room temperature for 5 min, while solution B, containing 250 μL of DMEM medium and 6 μL of siRNA, was prepared separately. Solution A and solution B were combined and allowed to stand at room temperature for 20 min. The resulting mixture was added to six-well plates, followed by supplementation with pure culture medium to achieve a final volume of 2 mL. After 6 h, a fresh culture medium containing 10% FBS was introduced for further cell culture.

2.5. In vitro characterization of Møm-coated PB (MPB) NPs

2.5.1. Immune escape behavior

Macrophages were seeded in 24-well plates and divided into two groups: the PB^{Rho} (containing rhodamine B-labeled PB NPs) group and the MPB^{Rho} (containing rhodamine B-labeled MPB NPs) group. Subsequently, the macrophages were incubated with different concentrations of rhodamine B-labeled NPs (10, 20, and 30 μg/mL for PB NPs) for a period of 4 h. Following the incubation, the cells were stained with 4′,6-diamidino-2-phenylindole (DAPI) for 5 min and then observed under a CLSM.

2.5.2. Cell uptake behavior

Macrophages were cultured in 24-well plates to investigate the real-time cellular uptake and trafficking of MPB^{Rho} NPs into lysosomes. Initially, macrophages were incubated with Hcy for 24 h, followed by the addition of MPB^{Rho} NPs at 0, 2, 4, and 6 h. Subsequently, the cells were treated with 1 μM Lyso-Tracker (C1047S; Beyotime, Shanghai, China) for 1 h and then stained with DAPI for 5 min. Lastly, the cells were observed and analyzed using CLSM.

To investigate the potential of Møm coating in promoting the recruitment of PB NPs by endothelial cells, endothelial cells were seeded in 24-well plates and divided into two groups: PB^{DiD} (DiD-labeled PB NPs) and MPB^{DiD} (DiD-labeled MPB NPs). After 24 h of induction with Hcy, PB^{DiD} NPs and MPB^{DiD} NPs were added to the cell culture medium and incubated at 4 °C for 4 h. Subsequently, the cells were fixed, and immunofluorescence staining was performed using the primary antibody ICAM-1 (ab171123; Abcam, Cambridge, UK). The cells were then visualized using CLSM.

2.5.3. Phagocytosis of NPs in co-cultured cells

The uptake ability of co-cultured endothelial cells and macrophages towards NPs was investigated following a previously described method [18]. In this study, endothelial cells were cultured in the upper layer, whereas macrophages were cultured in the lower layer of the coculture chamber. The cells were divided into two groups: the PB^{Rho} group and the MPB^{Rho} group. After 24 h of Hcy induction, different types of NPs were added to the coculture chamber and treated for 4 h. Subsequently, the cells were stained with DAPI for 5 min. Fluorescence images of endothelial cells and macrophages were acquired separately, and finally, the images from the two layers were merged to obtain a superimposed image using CLSM.

2.6. In vitro anti-atherosclerosis effect and mechanism

Macrophages were divided into several experimental groups: the control group, Hcy group (treated with 200 μM Hcy), PB group (treated with Hcy and 5 μg/mL PB NPs), RVS group (treated with Hcy and 5 μM RVS), and MPR group (treated with Hcy and 5 μM MPR NPs) [19].

2.6.1. Flow cytometry

Macrophages were cultured in six-well plates. After 24 h of treatment with Hcy and different NPs, the culture medium was removed, and the cells were subsequently treated with a ROS probe. After 30 min, the macrophages were detached using trypsin without phenol red and ethylenediaminetetraacetic acid (EDTA) for 1 min. The resulting cells were then centrifuged at 800 r/min for 5 min, followed by washing with phosphate-buffered saline (PBS) and another round of centrifugation. After resuspending the cells in PBS, the number of ROS-positive cells was evaluated using flow cytometry (Accuri C6 Plus; Becton, Dickinson and Company, Franklin, NJ, USA).

2.6.2. Cellular uptake of oxidized low-density lipoprotein (ox-LDL) and Oil red O (ORO) stained

Macrophages were cultured in 24-well plates and pre-treated with 200 μM Hcy and MPR NPs for 24 h. Subsequently, DiL-ox-LDL was added to achieve a final concentration of 40 μg/mL. After 4 h of incubation, macrophages were stained with DAPI for 5 min and visualized using a 60× oil objective under a CLSM (FV1200; Olympus).

Macrophages were seeded in 12-well plates to investigate the internalization of ox-LDL. After culturing the macrophages induced by Hcy for 24 h, ox-LDL (at a concentration of 80 μg/mL) and nano-drugs were added and incubated in a serum-free medium for 24 h. The residual medium was then washed off using PBS. Subsequently, the cells were incubated with 0.3% ORO (O1516; Sigma-Aldrich) for 30 min, followed by a rinsing step with 60% isopropanol for 5 s. Finally, the cells were observed under an inverted microscope (IX-73; Olympus).

2.6.3. RNA-sequencing (RNA-seq) analysis

Macrophages were divided into two groups: the control group and the Hcy group, with and without Hcy induction for a duration of 24 h, respectively. Total RNA was extracted from each group ($n = 3$) and sent to Biomarker Technologies (Beijing, China) for RNA-seq analysis.

Enrichment values were calculated as follows: enrichment values $= (n_{DEGs}/n_{total\ genes})/(n_{total\ DEGs}/n_{all\ genes})$. n_{DEGs} stands for the number of differentially expressed genes (DEGs) annotated to a pathway; $n_{total\ genes}$ stands for the total number of genes annotated to a pathway; $n_{total\ DEGs}$ stands for the number of all DEGs with Kyoto Encyclopedia of Genes and Genomes (KEGG) pathway annotation; and $n_{all\ genes}$ stands for the number of all genes annotated with KEGG pathway.

2.6.4. Western blotting assay

The cultured macrophages were treated with Hcy and nano-drugs for 24 h. After treatment, the cells were incubated on ice with a radio immunoprecipitation assay (RIPA) buffer containing PMSF, protease inhibitors, and phosphatase inhibitors for 30 min. The cell lysates were then centrifuged at 12,000 r/min for 30 min to obtain the supernatants. 30 μg of proteins were loaded onto an SDS-PAGE gel. Electrophoresis was performed at 80 V for 1 h, and the proteins were subsequently transferred to a polyvinylidene fluoride (PVDF) membrane at 200 mA for 2 h. The membrane was then blocked with a skim milk solution for 2 h. Primary antibodies against HIF-1α (20960-1-AP; Proteinch, Wuhan, China), TLR4 (SC-293072; Santa Cruz Biotechnology, Dallas, TX, USA), MyD88 (23230-1-AP; Proteinch), nuclear factor-kappaB (NF-κB) (BF8005; Affinity Biosciences, Changzhou, China), NLRP3 (bs-24563R; Bioss, Beijing, China), ASC (10500-1-AP; Proteinch), pro-caspase-1 (M025280; Abmart, Shanghai, China), caspase-1 (22915-1-AP; Proteinch), cleaved GSDMD (C-GSDMD) (10137, Cell Signaling, Danvers, MA, USA), IL-1β (AF-5103; Affinity Biosciences), and IL-18

(M027275; Abmart) were incubated with the membrane overnight at 4 °C. The PVDF membrane was then incubated with secondary antibodies for 2 h at room temperature. Finally, the membrane was developed and imaged after washing with PBS.

2.6.5. Immunofluorescence

Macrophages were cultured on confocal dishes and fixed with 4% paraformaldehyde for 30 min. To block the peroxidase activity of macrophages, 3% hydrogen peroxide was applied for a 10 min incubation. After three washes with PBS, the cells were permeabilized with an immunostaining permeabilization solution for 10 min. Subsequently, 5% goat serum was added to the cells to block nonspecific antigens for 30 min. The primary antibodies specific to adenosine triphosphate (ATP)-binding cassette transporter A1 (ABCA1) (bs-23418R; Bioss), ATP binding cassette transporter G1 (ABCG1) (13578-1-AP; Proteintech), zonula occludens-1 (ZO-1) (cl594-21773; Proteinch), and occludin (cl488-27260; Proteinch) were incubated with the macrophages overnight. Following the primary antibody incubation, fluorescence secondary antibodies were applied and incubated with the cells for 2 h. Finally, DAPI was used to stain the nuclei for 5 min, and the samples were imaged using a Nikon (Ti-E + A1 MP; Tokyo, Japan) confocal microscope.

2.6.6. Enzyme-linked immunosorbent assay (ELISA), total cholesterol (TC), and triglyceride (TG) assay

The anti-inflammatory effect of MPR NPs on macrophages was investigated using 24-well plates. After the cells adhered, Hcy and each nanodrug were added and incubated for 24 h. The levels of IL-1β (EMC001b; NeoBioscience, Shenzhen, China) and IL-18 (EMC011; NeoBioscience) were measured using ELISA kits. The serum levels of TC and TG were determined using TC (BC1985; Solarbio Science and Technology Co., Ltd.) and TG (BC0625; Solarbio Science and Technology Co., Ltd.) kits.

2.7. In vivo characterization

2.7.1. Experimental animals

$ApoE^{-/-}$ mice were obtained from Weishang Lituo Technology Co., Ltd. (Beijing, China) and housed in specific pathogen-free (SPF) conditions throughout the study. All animal care and experimental procedures followed the Animal Management Rules of the Ministry of Health of the People's Republic of China and were approved by the Animal Care Committee of Ningxia Medical University (License No.: 2018-047).

2.7.2. In vivo circulation time test and targeting of the atherosclerotic plaque

Serum samples were obtained from 6-week-old male C57BL/6 mice at various time points (0, 0.5, 1, 2, 4, 8, 12, and 24 h) following intravenous injection of ICG-labeled PB NPs (PB^{ICG} NPs) and ICG-labeled MPB NPs (MPB^{ICG} NPs) via the tail vein. The fluorescence signal intensities of the samples were measured using an small animal in vivo imaging system (IVIS); Lumina XR, New York City, NY, USA) spectrum system.

After a 12-week HMD, $ApoE^{-/-}$ mice were intravenously administered with PBS, PB^{ICG} NPs, and MPB^{ICG} NPs (ICG, 5 mg/kg) and sacrificed after 12 h. The aortas and other organs were collected for NPs distribution analysis using an IVIS spectrum system.

2.8. In vivo anti-atherosclerosis study

2.8.1. Feeding and treatment programs

Male mice, aged 6 weeks, were fed a HMD consisting of 1.7% methionine, 20% protein, 4.5% fat, and 55.5% carbohydrate for a duration of eight weeks. Subsequently, the mice were randomly divided into five groups, with six mice in each group. The groups were as follows: the control group (receiving a normal diet), the HMD group (receiving HMD with PBS treatment), the PB group (receiving HMD with 5 mg/kg PB NPs treatment), the RVS group (receiving HMD with 5 mg/kg RVS treatment), and the MPR group (receiving HMD with 5 mg/kg MPR NPs treatment). Each mouse in the study was administered intravenously via the tail vein twice weekly for a period of 10 weeks.

2.8.2. Metabolomics and gut microbiota analysis

Serum and fecal samples were collected from mice in the control, HMD, and MPR groups for long-read single-molecule sequencing (LM-SM) experiments and 16S rDNA sequencing ($n = 4$). The sequencing was performed by Novogene Technology Co., Ltd. (Beijing, China).

2.8.3. ORO staining and aorta tissues histological study of $ApoE^{-/-}$ mice

After a 10-week treatment period, $ApoE^{-/-}$ mice were euthanized. The entire aortas of three mice in each group were collected for longitudinal ORO staining, while the remaining three mice were used for aortic sections. Cryosections of the aortic root, aortic arch, and abdominal aorta were stained with ORO, hematoxylin/eosin (H&E), and Masson according to the provided kit instructions (G1346; Solarbio Science and Technology Co., Ltd.).

For immunohistochemistry analysis, the tissue sections were subjected to a series of sequential treatments, including peroxidase blocker, avidin, and biotin. Primary antibodies (F4-80) (28058-AP; Santa Cruz Biotechnology), matrix metalloprotein 9 (MMP-9) (10375-2-AP; Proteintech), CD31 (11265-1-AP; Proteintech), and α-smooth muscle actin (α-SMA) (55135-AP; Proteintech) were then applied to the sections. After that, secondary antibodies were added and incubated for 30 min. Finally, the sections were mounted with neutral resin and examined under a microscope (IX-73; Olympus).

2.9. The safety evaluation of MPR NPs

MPR NPs at different concentrations (10, 20, and 30 μg/mL) were incubated at 37 °C for 6 h with 4% (V/V) red blood cells. Following incubation, the samples were centrifuged at 3,500 r/min for 5 min to collect supernatants, and the corresponding absorbance values were measured at 540 nm. To evaluate the effects of NPs on erythrocyte morphology, the samples were treated with the highest concentration of MPR NPs (30 μg/mL) for 4 h.

After 24 h, RAW264.7, HUVECs, VSMCs, and HL7702 cells were treated with different concentrations (10, 20, and 30 μg/mL) of MPR NPs for safety evaluation. Cell viability was assessed using the Cell Counting Kit-8 (CCK-8) assay.

2.10. Statistical analysis

Data analysis was performed using GraphPad Prism version 9.4.1. All data were presented as mean ± standard deviation (SD). The Pearson product-moment correlation coefficient analysis (PCCs) was utilized to evaluate the colocalization intensity. For comparisons between the two groups, the t-test was employed. One-way analysis of variance (ANOVA) was used for comparisons among multiple groups, followed by the post-hoc least significant difference (LSD)-t test for further pairwise comparisons. Statistical significance was defined as $P < 0.05$.

3. Results and discussion

3.1. Preparation and characterization of MPR NPs

The TEM images revealed the uniform dispersion and cubic structure of the RVS-loaded PB (PR) NPs, having a size of 100 nm (Fig. 1A). Interestingly, after being coated with Møm, the PR NPs exhibited a surrounding membranous structure of approximately 10 nm, which resembled the thickness of 1−2 layers of the cell membrane [20] (Fig. 1B). DLS analysis consistently showed that the particle sizes of PR NPs and MPR NPs were 117 nm ± 17 nm and 120 nm ± 14 nm, respectively (Fig. 1C). These findings were consistent with the observations from the TEM images. Furthermore, the zeta-potential values of PB NPs, PR NPs, and MPR NPs were determined to be −8.35 ± 0.13, −11.43 ± 0.55, and −14.58 ± 0.28 mV, respectively (Fig. 1D).

To validate the successful coating of PB NPs by Møm, Coomassie brilliant blue staining clearly demonstrated the similarity between the protein bands of MPR NPs and pure Møm (Fig. 1E). In addition, Western blot analysis further confirmed the presence of the specific marker protein CD11b in MPR NPs, similar to that in natural Møm (Fig. 1F). To evaluate the co-localization of Møm and PB NPs, the Møm was labeled with DiL (green fluorescence) and PB NPs were labeled with DiD (red fluorescence), and the two were mixed with ultrasonic treatment. The resulting image, represented in Fig. 1G, demonstrated a perfect colocalization of the two colors. Optimization of the mass ratios of PB NPs and RVS revealed that the best EE (88.2% ± 0.2%) and LE (44.1% ± 0.1%) were achieved at a PB:RVS mass ratio of 1:1, as compared to ratios of 2:1 and 1:2 (Fig. 1H). Consequently, this ratio was determined to be the most effective while reducing the amount of PB NPs and RVS as much as possible. FT-IR spectra provided direct evidence for the successful loading of RVS into PB NPs, as it showed the presence of the $Fe^{2+}−CN−Fe^{3+}$ peak at 2,085 cm^{-1} in PB NPs, along with the characteristic peaks of RVS (C=C, $(CH_3)_2$CH, and S=O) in the PR NPs (Fig. 1I).

3.2. In vitro cellular uptake capacity

The coating of Møm plays a crucial role in preventing the phagocytosis of NPs by macrophages, thereby evading immune clearance *in vivo* [21]. As illustrated in Figs. 2A and B, the red fluorescence signal of macrophages treated with MPB^{Rho} NPs was significantly lower compared to those treated with PB^{Rho} NPs. This phenomenon remained consistent even at high concentrations, highlighting the effectiveness of the Møm coating in preventing macrophage phagocytosis of PB NPs. In addition, within the intracellular environment, lysosomes act as "digestive organs" capable of degrading and eliminating nanodrugs, consequently reducing their therapeutic efficacy. By monitoring the fate of MPB NPs upon entering Hcy-induced macrophages, we observed that MPB^{Rho} NPs (red fluorescence) were present in the macrophages after 2 h. Subsequently, a portion of these NPs entered lysosomes labeled with Lyso-Tracker (green fluorescence) (Fig. 2C). Moreover, macrophages exhibited a strong uptake of MPB^{Rho} NPs at 4 h, and partial red fluorescence was observed in the cytoplasm at 4 and 6 h, indicating that MPB^{Rho} NPs could bypass lysosomes to some extent upon cellular internalization (Figs. 2D and E). These findings suggest that MPB^{Rho} NPs can effectively minimize drug degradation within the acidic lysosomal environment, enhancing their overall efficacy.

During the development of atherosclerosis, Hcy-induced damage to endothelial cells leads to the secretion of the adhesion molecule ICAM-1, which in turn recruits macrophages [22]. As anticipated, we observed a robust green fluorescence signal of ICAM-1 in endothelial cells. Moreover, the red fluorescence signal

in cells treated with MPB^{DiD} NPs was significantly higher than that in cells treated with PB^{DiD} NPs, suggesting an interaction between ICAM-1 and Møm (Figs. 2F and G). These findings indicate that damaged endothelial cells can effectively recruit MPB NPs. Additionally, atherosclerotic plaques in inflammatory conditions are known to possess a slightly acidic environment compared to the normal physiological environment. To explore the release behavior of RVS from MPR NPs, we compared the release profiles at pH 6.8 and pH 7.4 (Figs. 2H). Consistently, we observed a higher release of RVS from MPR NPs at pH 6.8. Collectively, these results highlight the unique characteristics of MPR NPs, enabling their enhanced accumulation at the plaque site and improved therapeutic efficacy in the treatment of atherosclerosis.

In this study, we employed a transwell chamber system to simulate the atherosclerotic plaque environment by co-culturing endothelial cells and macrophages in the presence of Hcy (Figs. 2I). By comparing the uptake ability of these cells, Figs. 2J and K demonstrated a stronger red fluorescence signal in the MPB^{Rho} group, indicating higher uptake in macrophages and endothelial cells compared to the PB^{Rho} group. Importantly, macrophages in the MPB^{Rho} group exhibited significantly higher uptake than endothelial cells. These findings suggest that MPB NPs are more likely to be taken up by macrophages in an Hcy-induced environment, benefiting from the targeting and "homing effect" of Møm [23]. Additionally, this result indicates that the excellent permeability of MPR NPs may contribute to their retention at the atherosclerotic site.

3.3. Targeted delivery in HHcy-induced ApoE$^{−/−}$ mice

Inspired by the remarkable immune evasion ability of MPR NPs and their high uptake by Hcy-induced cells *in vitro*, we conducted experiments to assess the circulation time of MPB NPs in C57BL/6 mice and their targeting ability towards atherosclerotic plaques in *ApoE$^{−/−}$* mice under conditions of HHcy. By comparing the fluorescence intensity in the bloodstream, we observed that the MPB^{ICG} group exhibited a significantly prolonged half-life ($t_{1/2}$) compared to the PB^{ICG} group ($t_{1/2} \approx 1.482$ h for PB^{ICG} group vs. $t_{1/2} \approx 3.518$ h for MPB^{ICG} group) (Figs. 3A and B). Moreover, the fluorescence intensity throughout the entire aorta was noticeably increased in the MPB^{ICG} group (Figs. 3C and D) in comparison to the PB^{ICG} group. These findings confirmed the capacity of MPB NPs to enhance the $t_{1/2}$ of blood circulation and facilitate drug accumulation within atherosclerotic plaques, owing to the Møm coating [24]. Notably, the fluorescence intensity in the liver was reduced in the MPB^{ICG} NPs-treated mice compared to the PB^{ICG} NPs-treated group (Figs. 3E and F). This distribution pattern is advantageous in reducing drug clearance, improving the bioavailability of MPB NPs in atherosclerosis, and mitigating liver injury associated with excessive accumulation of PR NPs.

3.4. The therapeutic effect on HHcy-induced atherosclerosis of MPR NPs

The impact of MPR NPs on the development of atherosclerosis in *ApoE$^{−/−}$* mice fed a HMD was evaluated by assessing plaque area, serum TC, TG, and Hcy levels, as well as plaque stability. Analysis of ORO staining revealed a substantial increase in plaque area in the aorta of the HMD group compared to the control group (20.90% ± 2.54% vs. 0.30% ± 0.13%). However, following treatment with PB NPs, RVS, and MPR NPs, the plaque area of PB NPs, RVS, and MPR NPs treatment was measured as 11.82% ± 0.81%, 6.98% ± 0.52%, and 1.53% ± 1.25%, respectively (Figs. 4A and B). Similarly, the highest plaque areas were observed in the aortic root of the HMD group (41.51% ± 2.75%), but after treatment with PB NPs, RVS, and MPR NPs, the plaque areas were measured as 31.33% ± 3.20%,
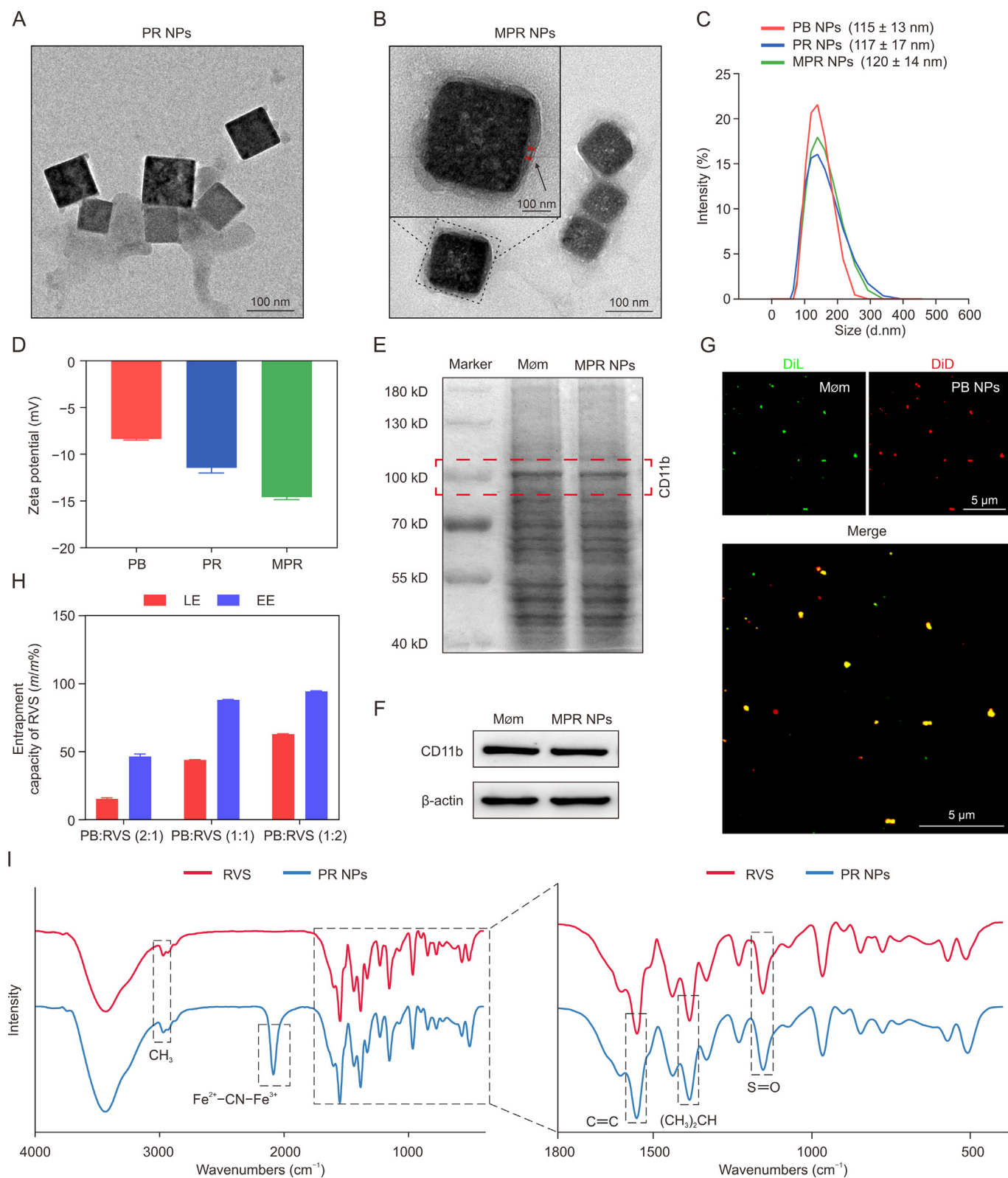
Fig. 1. Fabrication and characterization of macrophage membrane (Møm)-coated rosuvastatin (RVS)-loaded Prussian blue (PB) nanoparticles (MPR NPs). (A, B) Transmission electron microscope (TEM) images of RVS-loaded PB NPs (PR NPs) (A) and MPR NPs (B) (inset: magnified MPR NPs image). (C) Dynamic light scattering (DLS) analysis of PB NPs, PR NPs, and MPR NPs. (D) Zeta potentials of PB NPs, PR NPs, and MPR NPs. (E) Coomassie brilliant blue stain analysis of Møm and MPR NPs proteins. (F) Western blot assay of characteristic marker cluster of differentiation 11b (CD11b) in the Møm and MPR NPs. (G) Fluorescence imaging of a mixture of Møm and PB NPs. (H) The effect of PB NPs and RVS with different proportions (2:1, 1:1, and 1:2) on encapsulation efficiency (EE)/loading efficiency (LE). (I) Fourier transform infrared spectroscopy (FT-IR) spectra of RVS and PR NPs, and the amplification of selected region. DiL: 1,1-dioctadecyl-3,3,3,3-tetramethylindocarbocyanine perchlorate; DiD: 1,1-dioctadecyl-3,3,3,3-tetramethylindodicarbocyanine perchlorate.
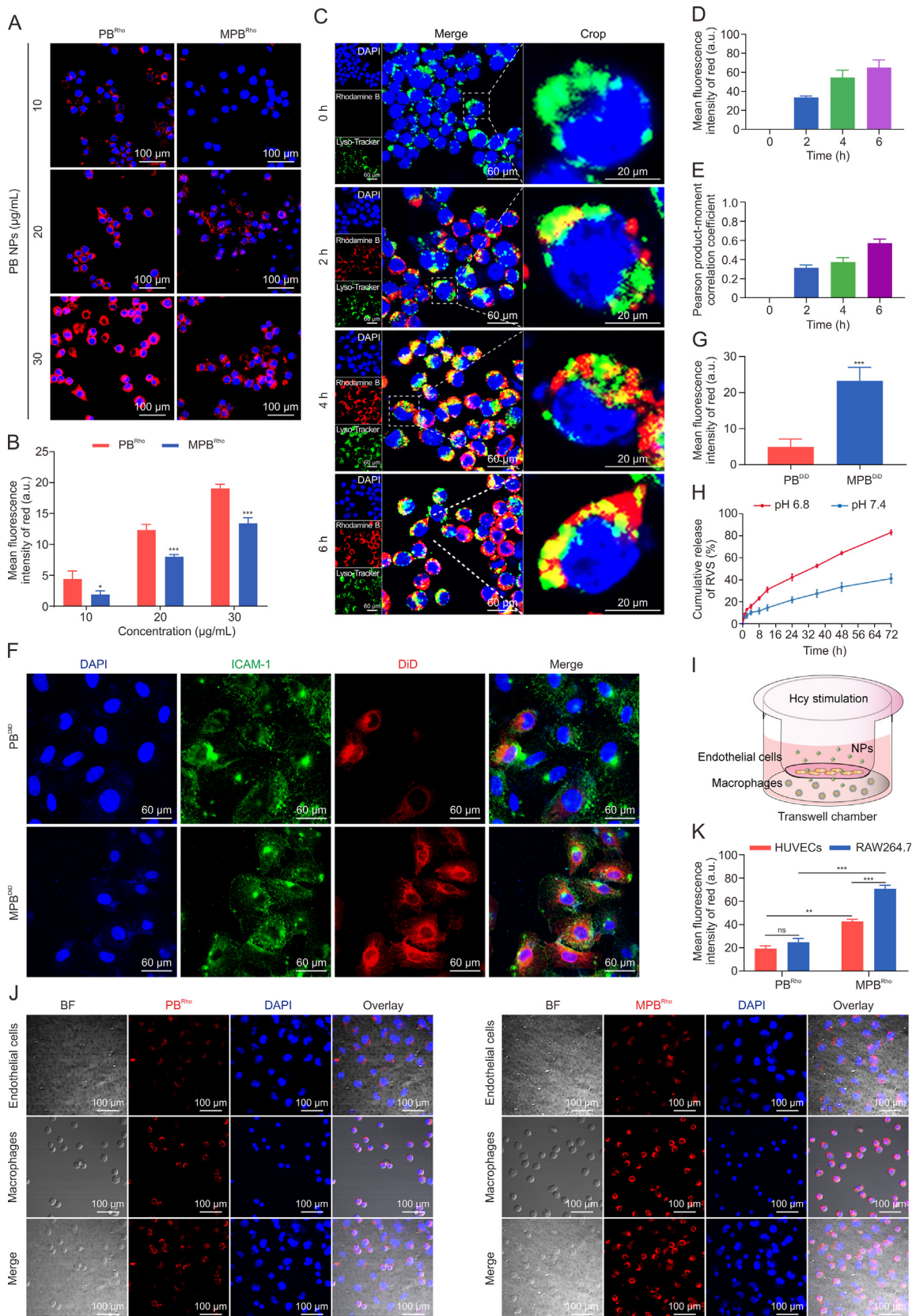
Fig. 2. Uptake and target ability evaluation of macrophage membrane (Møm)-coated Prussian blue (PB) nanoparticles (MPB NPs) to homocysteine (Hcy)-induced macrophages. (A) Fluorescence images of the immune evading ability of rhodamine B-labeled PB (PB^Rho) NPs and rhodamine B-labeled Møm-coated PB (MPB^Rho) NPs. (B) Quantification of rhodamine B fluorescence intensity. (C) Confocal fluorescence microscopy imaging of cells uptake ability and subcellular localization of MPB NPs for different times. (D, E) Quantification of red fluorescence intensity (D) and pearson product-moment correlation coefficient (E) between rhodamine B and Lyso-Tracker fluorescence. (F) Representative fluorescence images of Hcy treated endothelial cells incubating with 1,1-dioctadecyl-3,3,3,3-tetramethylindodicarbocyanine perchlorate (DiD)-labeled PB (PB^DiD) NPs and DiD-labeled MPB (MPB^DiD) NPs

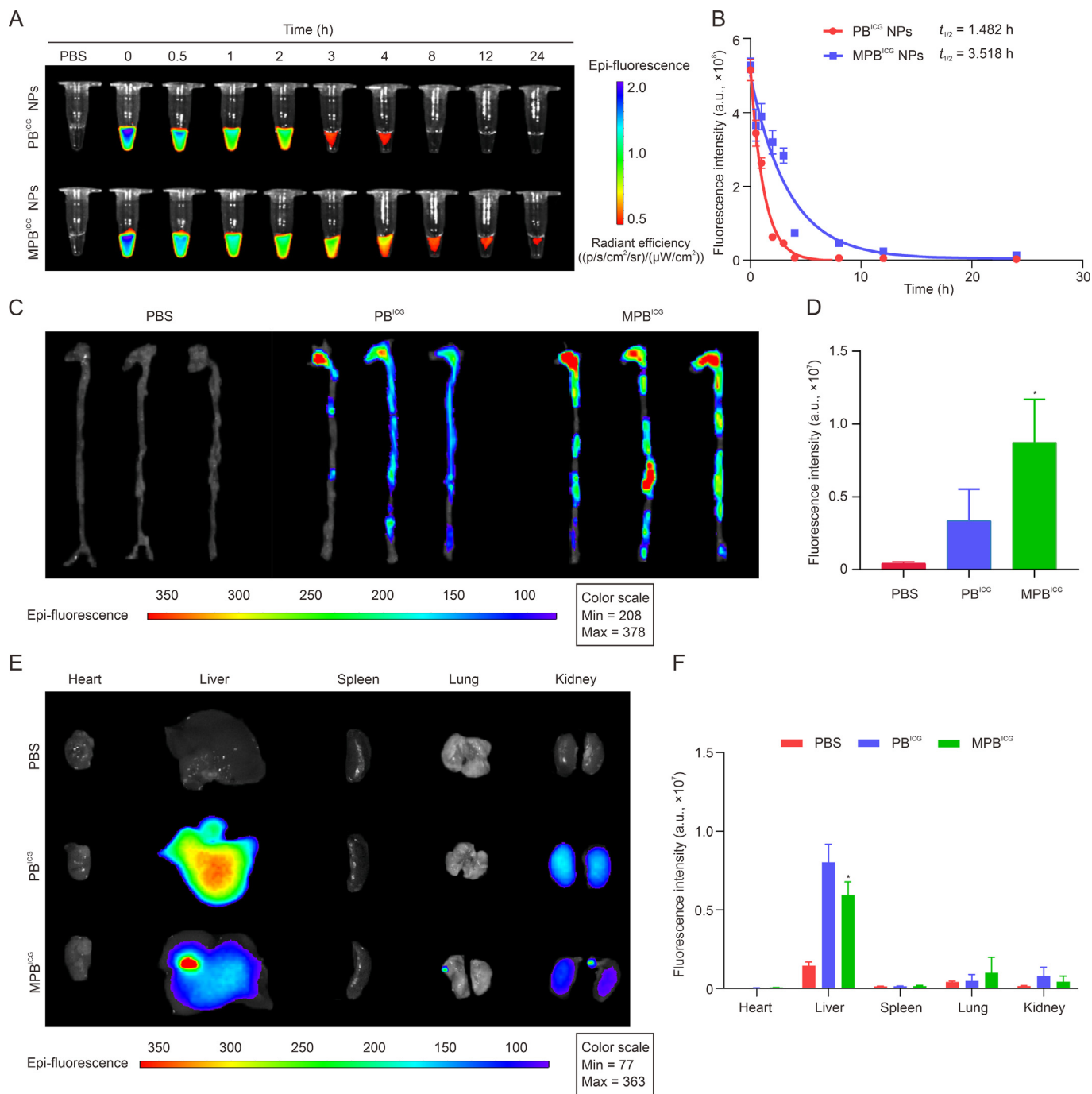**Fig. 3.** Circulation and targeting ability of macrophage membrane (Møm)-coated Prussian blue (PB) nanoparticles (MPB NPs) in the apolipoprotein E knockout ($ApoE^{-/-}$) mice after i.v. administration. (A) Fluorescence images of indocyanine green (ICG)-labeled PB (PB^{ICG}) NPs and ICG-labeled Møm-coated PB (MPB^{ICG}) NPs in the serum at different time points. (B) Pharmacokinetic curves of PB^{ICG} NPs and MPB^{ICG} NPs in C57BL/6 mice. (C, D) The fluorescence images (C) and quantitative analysis (D) of the aortas of $ApoE^{-/-}$ mice. (E, F) The fluorescence images (E) and quantitative analysis (F) of the major organs excised from the $ApoE^{-/-}$ mice. Data are means ± standard deviation (SD) ($n = 3$). $^*P < 0.05$ vs. the PB^{ICG} group. PBS: phosphate-buffered saline; $t_{1/2}$: half-life.

19.46% ± 2.65%, and 12.63% ± 2.55%, respectively (Figs. 4C and D). Moreover, mice treated with MPR NPs exhibited a significant reduction in plaque area in the aortic arch and abdominal aorta (Figs. 4E−H). Furthermore, Figs. 4I−K demonstrated that MPR NPs

effectively reversed the upregulation of TC, TG, and Hcy in the serum of $ApoE^{-/-}$ mice fed a HMD.

Plaque stability was also assessed using various indicators. H&E staining revealed that treatment with MPR NPs significantly

for 24 h. (G) Quantification of DiD fluorescence intensity. (H) The cumulative release of RVS from MPR NPs at different pH values. (I) Schematic diagram of transwell model. (J) Phagocytosis of fluorescent PB^{Rho} NPs and MPB^{Rho} NPs in co-cultured macrophages and endothelial cells in transwell chambers. (K) Quantitative of rhodamine B fluorescence intensity in macrophages and endothelial cells. Data are means ± standard deviation (SD) ($n = 3$). $^*P < 0.05$, $^{**}P < 0.01$, and $^{***}P < 0.001$ vs. the PB^{Rho}/PB^{DiD}. ns: no significance. DAPI: 4′,6-diamidino-2-phenylindole; PCCs: Pearson product-moment correlation coefficient analysis; BF: bright field; HUVEC: human umbilical vein endothelial cell line.
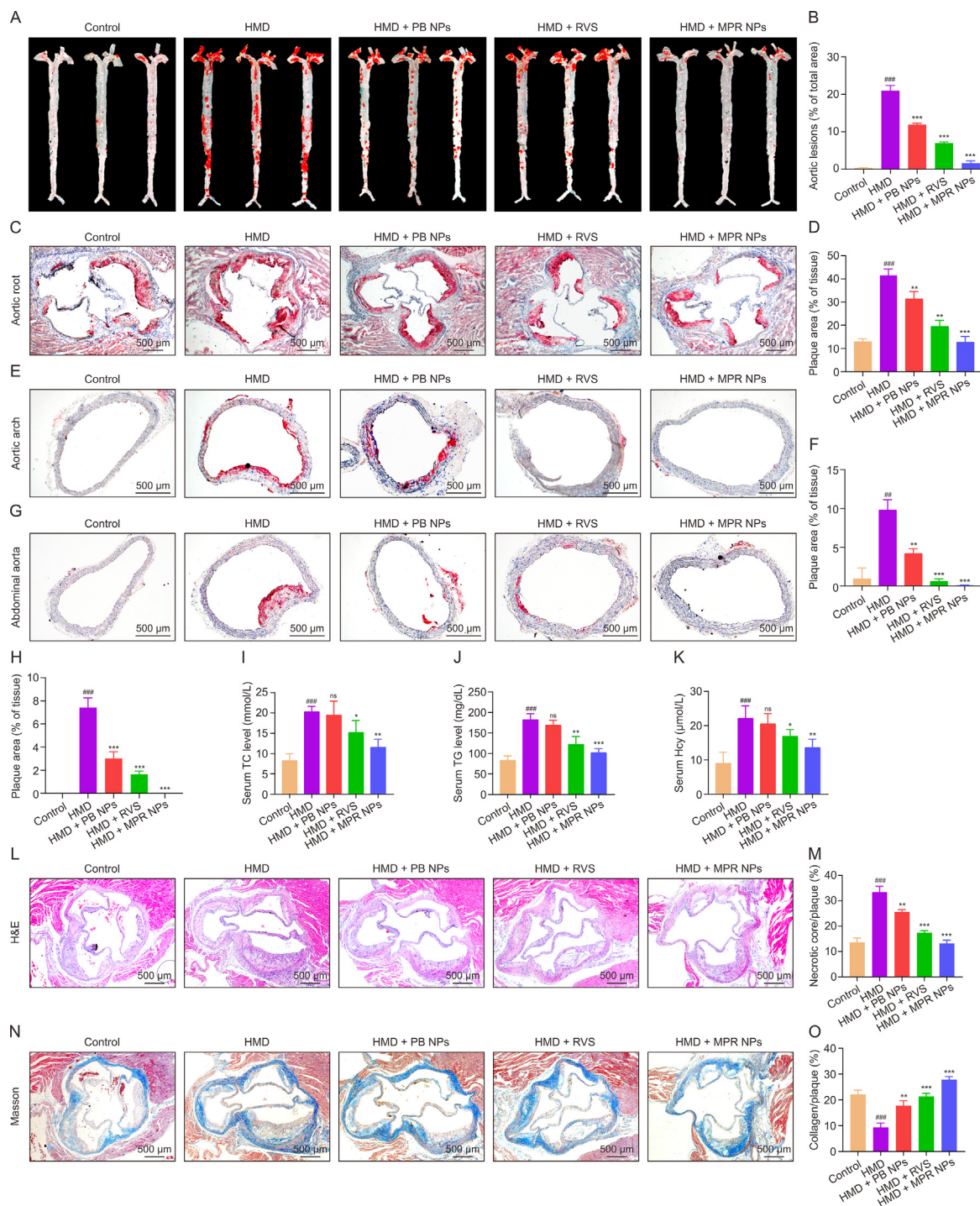
Fig. 4. The efficacy of macrophage membrane (Møm)-coated rosuvastatin (RVS)-loaded Prussian blue (PB) nanoparticles (MPR NPs) in apolipoprotein E knockout ($ApoE^{-/-}$) mice fed a high methionine diet (HMD). (A, B) Oil red O (ORO) staining (A) and quantitative analysis (B) of the aorta ($n = 3$). (C, D) ORO staining (C) and quantitative analysis (D) of aortic root. (E−H) ORO staining: the images (E) and quantitative analysis (F) of aortic arch, and the images (G) and quantitative analysis (H) of abdominal aorta. (I−K) The assay of total cholesterol (TC) (I), triglyceride (TG) (J), and Hcy (K) levels in the $ApoE^{-/-}$ mice serum ($n = 3$). (L−O) Hematoxylin/eosin (H&E) staining (L) and quantitative analysis (M) of aortic root, and Masson's trichrome (N) and quantitative analysis (O) of aortic root. Data are means ± standard deviation (SD) ($n = 3$). $^{\#\#}P < 0.01$ and $^{\#\#\#}P < 0.001$ vs. the control group; $^{*}P < 0.05$, $^{**}P < 0.01$, and $^{***}P < 0.001$ vs. the HMD. ns: no significance.

attenuated the lipid-enriched necrotic core in the plaque of the aortic root, as evidenced by the significant reduction in the expression of the macrophage marker F4/80 (Figs. 4L, 4M, S1A, and S1B). The formation of a necrotic core area by dead macrophages is closely associated with plaque development and the severity of atherosclerosis [25]. Neovascularization around the necrotic core, levels of MMP-9 expression, and the proliferation of smooth muscle cells within the plaque are known to correlate positively with plaque vulnerability [26]. Immunohistochemical staining demonstrated reduced levels of CD31-positive endothelial cells and MMP-

9 in the MPR group compared to the HMD group (Figs. S1C–F). Masson staining revealed an increase in collagen content and a decrease in the levels of α-SMA-positive VSMCs in the atherosclerotic plaque following treatment with MPR NPs (Figs. 4N, 4O, S1G, and S1H). These observations indicate that MPR NPs effectively enhance plaque stability by thickening the fibrous caps, thereby aiding in the prevention of thrombotic diseases.

It is worth noting that compared to oral administration of RVS, intravenous injection provides the advantage of rapidly introducing drugs into the bloodstream, thereby quickly producing therapeutic effects. This makes it particularly useful in cases of acute cardiovascular events or the need for rapid reduction of cholesterol levels. In this study, intravenous injection of MPR NPs used a lower dose compared to the RVS dose used for oral gavage in the mice by previous researchers [27]. However, the application of biomimetic membranes still faces significant challenges. Due to the characteristics of the human immune system, it is necessary to extract cell membranes from the patient's own body, which limits the implementation of intravenous injection of biomimetic nanodrugs.

3.5. MPR NPs inhibited Hcy-induced macrophage pyroptosis through TLR4/HIF-1α/NLRP3 signaling pathways

Hcy promotes macrophage pyroptosis through the TLR4/NLRP3 signaling pathway, as demonstrated by our recent study [28]. TLR4, a pattern recognition receptor, is known to play a crucial role in the activation of the NLRP3 inflammasome [29]. Based on this finding, we hypothesized that Hcy-induced pyroptosis in macrophages is mediated by the TLR4/NLRP3 pathway. To elucidate the underlying mechanism, we performed RNA-seq analysis, which revealed differential expression of a total of 4,250 genes upon exposure to Hcy (Fig. S2A). Notably, the TLR signaling pathway, NF-κB signaling pathway, and NOD-like receptor signaling pathway were prominently affected among these DEGs (Fig. S2B). Furthermore, the Gene Ontology (GO) analysis indicated that the inflammatory response and response to oxidative stress were among the biological processes influenced by Hcy (Fig. S2C), both of which are closely associated with pyroptosis. Consistently, gene set enrichment analysis (GSEA) revealed predominantly upregulated DEGs in these KEGG signaling pathways and GO categories (Fig. S2D). To investigate the involvement of TLR4 in the NLRP3 inflammasome pathway further, we conducted TLR4 knockdown experiments and monitored the protein levels of key pathway components. Interestingly, we observed a significant reduction in the levels of TLR4, NF-κB, NLRP3, and C-GSDMD in macrophages with TLR4 interference (Figs. S2E and F). Based on these findings, we can conclude that Hcy induces macrophage pyroptosis through the TLR4/NLRP3 signaling pathway. Overall, our study provides novel insights into the molecular mechanisms underlying Hcy-induced macrophage pyroptosis. The dysregulation of the TLR4/NLRP3 signaling pathway and the subsequent inflammatory response and oxidative stress play vital roles in this process. Further understanding of these mechanisms may lead to the development of potential therapeutic strategies for disorders associated with Hcy-induced pyroptosis.

We investigated the impact of MPR NPs on the expression of proteins involved in Hcy-induced macrophage pyroptosis. Our results demonstrated a significant decrease in the levels of TLR4, MyD88, and NF-κB in macrophages treated with MPR NPs compared to the Hcy group (Fig. S3). Moreover, Hcy exposure led to mitochondrial oxidative damage and ROS release, resulting in the upregulation of HIF-1α and activation of the NLRP3-regulated signaling pathway in pyroptosis [30,31]. Flow cytometry analysis revealed that the percentage of ROS-positive cells following Hcy

treatment was 37.10% ± 0.70%. However, treatment with PB NPs, RVS, and MPR NPs reduced the percentages of ROS-positive cells to 26.70% ± 2.25%, 21.03% ± 1.03%, and 9.50% ± 0.30%, respectively (Fig. 5A). Furthermore, Western blot analysis demonstrated a decrease in the expression of HIF-1α, NLRP3, and ASC upon treatment with MPR NPs (Fig. 5B), along with a downregulation of pro-caspase-1, caspase-1, and C-GSDMD (Fig. 5C). Immunofluorescence staining indicated a significant reduction in the co-localization coefficient of NLRP3 (red fluorescence) and ASC (green fluorescence) in the MPR group compared to the Hcy group ($r = 0.45 \pm 0.16$ for Hcy + MPR group vs. $r = 0.74 \pm 0.02$ for Hcy group) (Figs. 5D and E). Similarly, the fluorescence intensity of caspase-1 (green fluorescence) and C-GSDMD (pink fluorescence) was decreased in macrophages treated with MPR NPs (Figs. 5F–I). Lastly, Western blotting and ELISA assays showed that MPR NPs treatment significantly inhibited the protein levels and extracellular contents of IL-18 and IL-1β (Figs. 5J and K). Previous studies have reported that PB NPs scavenge ROS to inhibit macrophage pyroptosis [32,33], while RVS inhibits this process through the TLR4/NF-κB/NLRP3 pathway [34]. Consistent with these findings, our MPR NPs, combining PB NPs and RVS, exhibited a synergistic effect in suppressing Hcy-induced macrophage pyroptosis, thereby alleviating the inflammatory response-driven acceleration of atherosclerosis. This study provides valuable insights into the inhibition of Hcy-induced macrophage pyroptosis and suggests a potential therapeutic strategy for mitigating atherosclerosis.

Next, we evaluated the impact of MPR NPs on plaque pyroptosis in $ApoE^{-/-}$ mice fed a HMD. Immunohistochemical staining showed a notable reduction in the levels of HIF-1α in atherosclerotic plaques following treatment with MPR NPs (Figs. 6A and B). Additionally, immunofluorescence staining was performed to examine the binding of NLRP3 and ASC in the plaques. As expected, the co-localization coefficient of NLRP3 and ASC was increased in the HMD group compared to the control group (0.82 ± 0.03 vs. 0.50 ± 0.04). However, treatment with PB NPs, RVS, and MPR NPs resulted in co-localization coefficients of 0.71 ± 0.02, 0.62 ± 0.06, and 0.46 ± 0.03, respectively (Figs. 6C and D). Moreover, immunofluorescence analysis demonstrated increased levels of C-GSDMD in F4/80 positive macrophages in the HMD group compared to the control group (21.11% ± 1.68% vs. 4.38% ± 0.44%), whereas PB NPs, RVS, and MPR NPs reduced these levels (12.84% ± 1.92%, 6.87% ± 0.60%, and 3.10% ± 0.47%, respectively) (Figs. 6E and F). Accordingly, our findings indicate that MPR NPs can effectively attenuate HMD-induced pyroptosis in $ApoE^{-/-}$ mice. These results provide compelling evidence for the ability of MPR NPs to modulate plaque pyroptosis in an *in vivo* setting and suggest their potential utility as a therapeutic intervention for atherosclerosis.

Abnormal expression of HIF-1α can disrupt cholesterol efflux by altering the localization of ABCA1 and ABCG1 in the plasma membrane [35,36]. To investigate the effect of MPR NPs on the expression of ABCA1 and ABCG1 in Hcy-induced macrophages, we performed immunofluorescence staining. As shown in Figs. 7A–D, the fluorescence intensity of ABCA1 (green fluorescence) and ABCG1 (red fluorescence) significantly decreased in the Hcy group, while their intensities gradually increased in the PB, RVS, and MPR groups. Furthermore, we examined the impact of MPR NPs on the lipid uptake ability of Hcy-induced macrophages. As depicted in Figs. 7E and F, the Hcy group exhibited the strongest red fluorescence signal, indicating a high uptake of ox-LDL. Conversely, the red signal intensity decreased sequentially in the PB, RVS, and MPR groups, suggesting reduced ox-LDL uptake. Likewise, ORO staining revealed a significant decrease in ox-LDL internalization in Hcy-induced foam cells treated with MPR NPs compared to the PB NPs and RVS groups, as evidenced by the reduced intensity of ORO
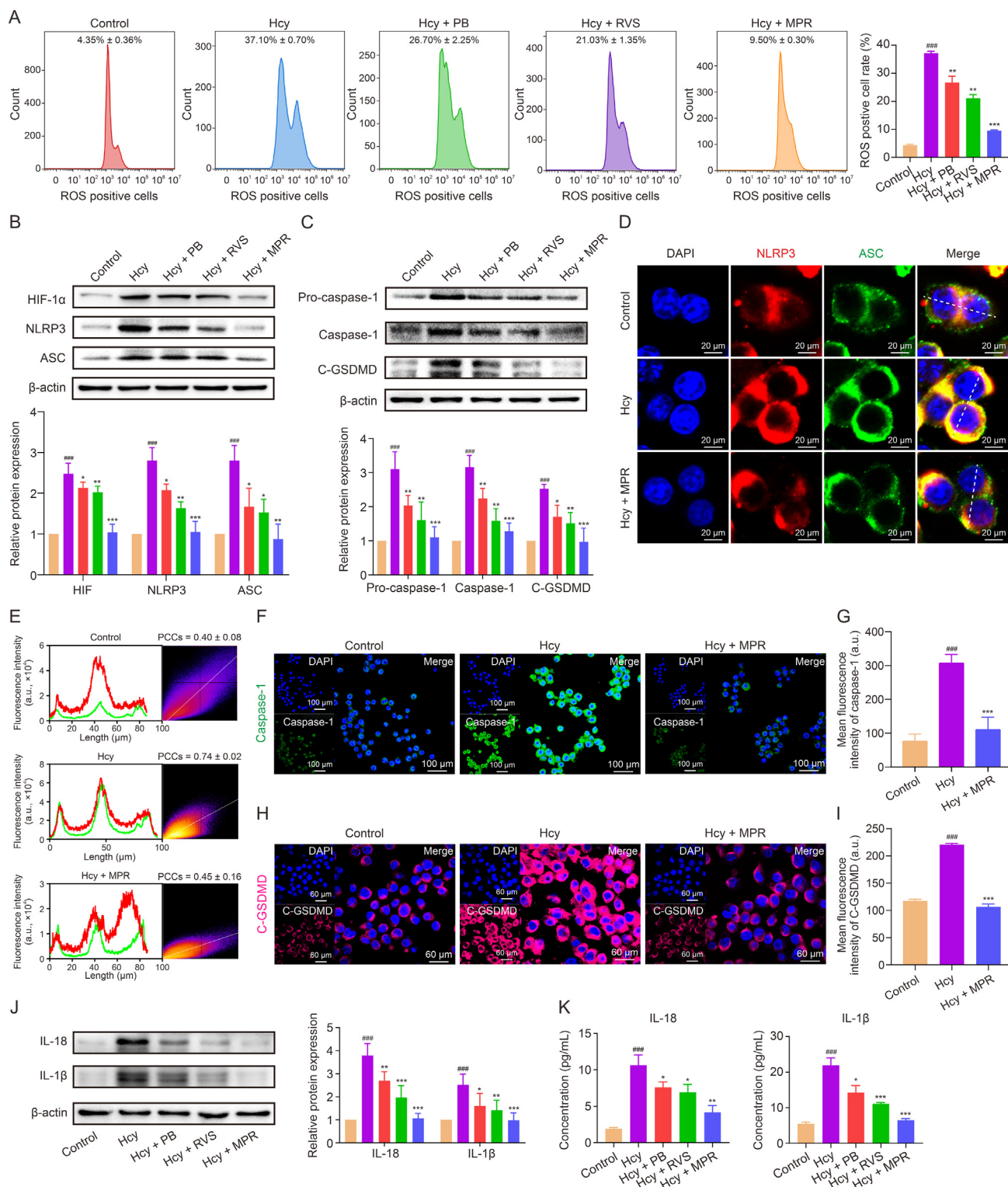
Fig. 5. Macrophage membrane (Møm)-coated rosuvastatin (RVS)-loaded Prussian blue (PB) nanoparticles (MPR NPs) inhibited pyroptosis in homocysteine (Hcy)-induced macrophages. (A) Flow cytometry and quantitative analysis of reactive oxygen species (ROS)-positive macrophages. (B) Western blot assay and quantification analysis of hypoxia-inducible factor-1 (HIF-1α), nucleotide-binding and oligomerization domain (NOD)-like receptor thermal protein domain associated protein 3 (NLRP3), and apoptosis-associated speck-like protein (ASC) levels. (C) Western blot assay and quantification analysis of pro-caspase-1, caspase-1, and cleaved-gasdermin D (C-GSDMD) protein expression. (D) Immunofluorescence images of NLRP3 and ASC colocalization. (E) Plot profile analysis of red and green fluorescence intensity and Pearson product-moment correlation coefficient analysis (PCCs). (F, G) Immunofluorescence images (F) and fluorescence intensity (G) of caspase-1. (H, I) Immunofluorescence images (H) and fluorescence intensity (I) of C-GSDMD. (J) Western blot assay and quantification analysis of interleukin (IL)-18 and IL-1β protein expression. (K) Enzyme-linked immunosorbent assay (ELISA) assay of inflammatory factor IL-18 and IL-1β. Data are means ± standard deviation (SD) ($n = 3$). $^{\#\#\#}P < 0.001$ vs. the control group; $^{*}P < 0.05$, $^{**}P < 0.01$, and $^{***}P < 0.001$ vs. Hcy. DAPI: 4′,6-diamidino-2-phenylindole.
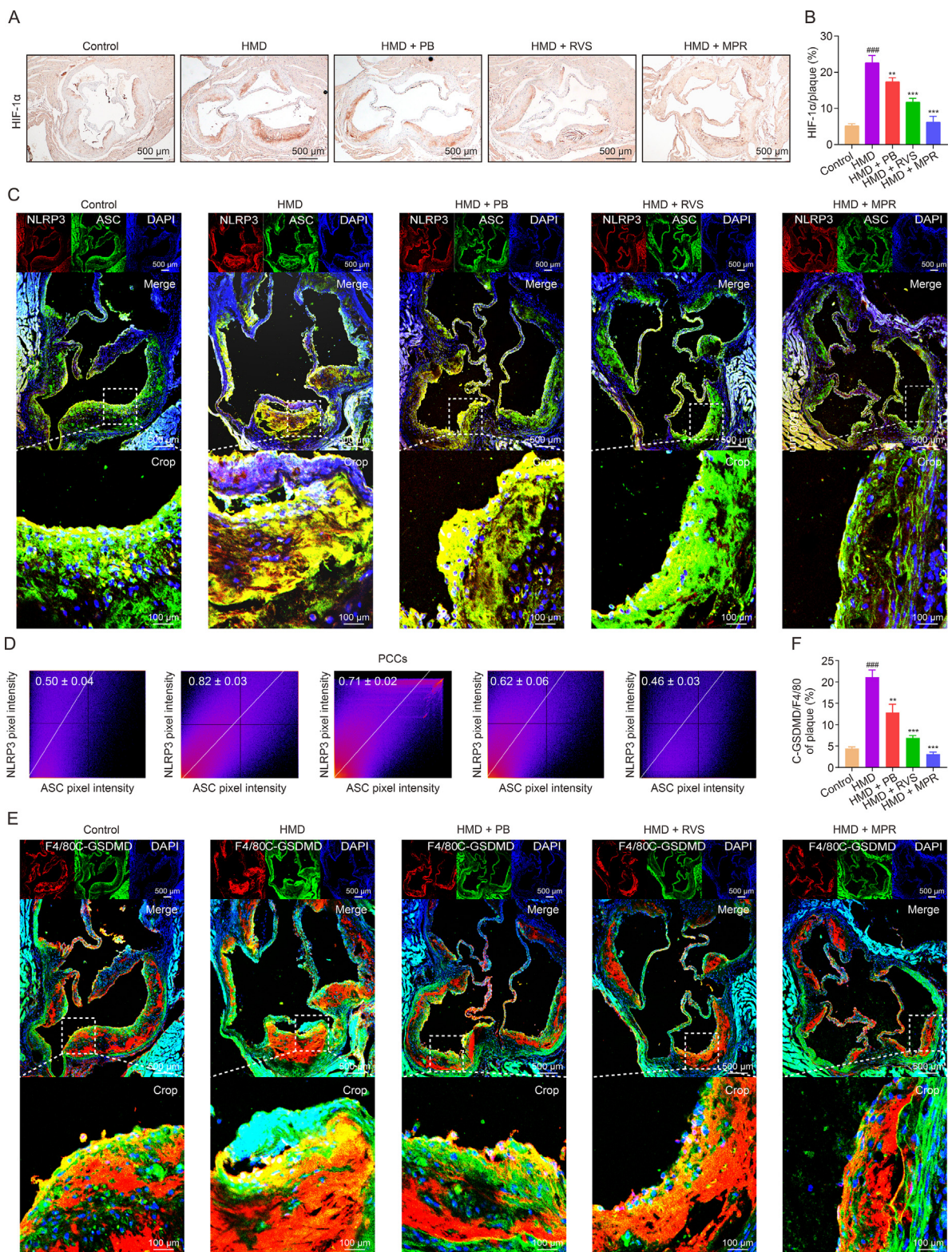
Fig. 6. Macrophage membrane (Møm)-coated rosuvastatin (RVS)-loaded Prussian blue (PB) nanoparticles (MPR NPs) inhibited pyroptosis in atherosclerosis plaque of apolipo-protein E knockout (*ApoE*$^{-/-}$) mice fed an high methionine diet (HMD). (A, B) Immunohistochemistry staining with antibody to hypoxia-inducible factor-1 (HIF-1α) (A) and quantitative analysis (B) of aortic roots. (C) Immunofluorescence images of nucleotide-binding and oligomerization domain (NOD)-like receptor thermal protein domain associated protein 3 (NLRP3) and apoptosis-associated speck-like protein (ASC) colocalization. (D) Pearson product-moment correlation coefficient analysis (PCCs) of NLRP3 (red) and ASC (green) colocalization. (E) Immunofluorescence images of cleaved-gasdermin D (C-GSDMD) and F4/80 levels. (F) Fluorescence intensity of C-GSDMD/F4/80. The above experiments were performed on HMD-induced *ApoE*$^{-/-}$ mice treated with PB NPs, RVS, and MPR NPs. Data are means ± standard deviation (SD) (*n* = 3). $^{###}P < 0.001$ vs. the control group; $^{**}P < 0.01$ and $^{***}P < 0.001$ vs. the HMD. DAPI: 4′,6-diamidino-2-phenylindole.
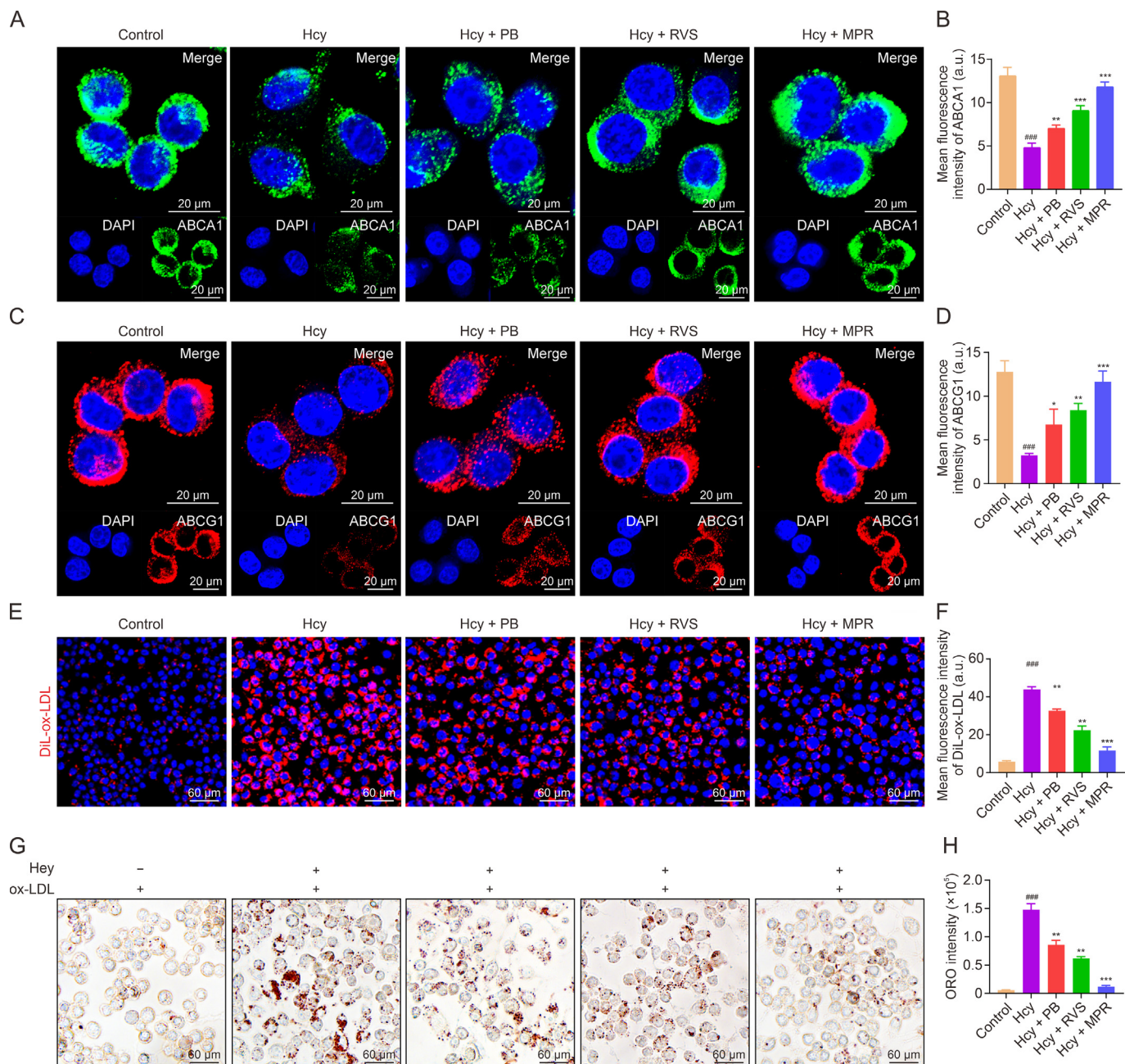
Fig. 7. Macrophage membrane (Møm)-coated rosuvastatin (RVS)-loaded Prussian blue (PB) nanoparticles (MPR NPs) upregulated adenosine triphosphate (ATP)-binding cassette transporter A1 (ABCA1)/ATP binding cassette transporter G1 (ABCG1) and inhabited lipid uptake in macrophages. (A, B) Immunofluorescence images (A) and fluorescence intensity quantification analysis (B) of ABCA1. (C, D) Immunofluorescence images (C) and fluorescence intensity quantification analysis (D) of ABCG1. (E) Cellular uptake of 1,1-dioctadecyl-3,3,3,3-tetramethylindocarbocyanine perchlorate (DiL)-oxidized low-density lipoprotein (ox-LDL). (F) Quantification of DiL-ox-LDL fluorescence intensity. (G, H) Oil red O (ORO) staining (G) and quantitative analysis (H). The above experiments were performed on homocysteine (Hcy)-induced macrophages treated with PB NPs, RVS, and MPR NPs. Data are means ± standard deviation (SD) ($n = 3$). $^{###}P < 0.001$ vs. the control group; $^{*}P < 0.05$, $^{**}P < 0.01$, and $^{***}P < 0.001$ vs. Hcy. DAPI: 4′,6-diamidino-2-phenylindole.

staining in macrophages (Figs. 7G and H). These findings suggest that MPR NPs can enhance cholesterol efflux by upregulating the expression of ABCA1 and ABCG1 while inhibiting lipid uptake and internalization in Hcy-induced macrophages. These effects are crucial in suppressing the formation of foam cells. Our results provide additional evidence supporting the potential of MPR NPs as a therapeutic approach to mitigate foam cell development and atherosclerosis progression. By promoting cholesterol efflux and inhibiting lipid uptake, MPR NPs offer a promising strategy for the treatment of atherosclerosis.

3.6. MPR NPs regulated the metabolism of HHcy-induced ApoE$^{-/-}$ mice

Metabolomics is a valuable technique for assessing the overall metabolic state in cells, tissues, or biological fluids and has emerged as a powerful tool for investigating the pathophysiology of atherosclerosis [37]. Principal component analysis (PCA) revealed significant differences in both positive and negative compounds among the control, MPR, and HMD groups (Fig. 8A). A volcano plot displayed the upregulation/downregulation of 79/51 positive
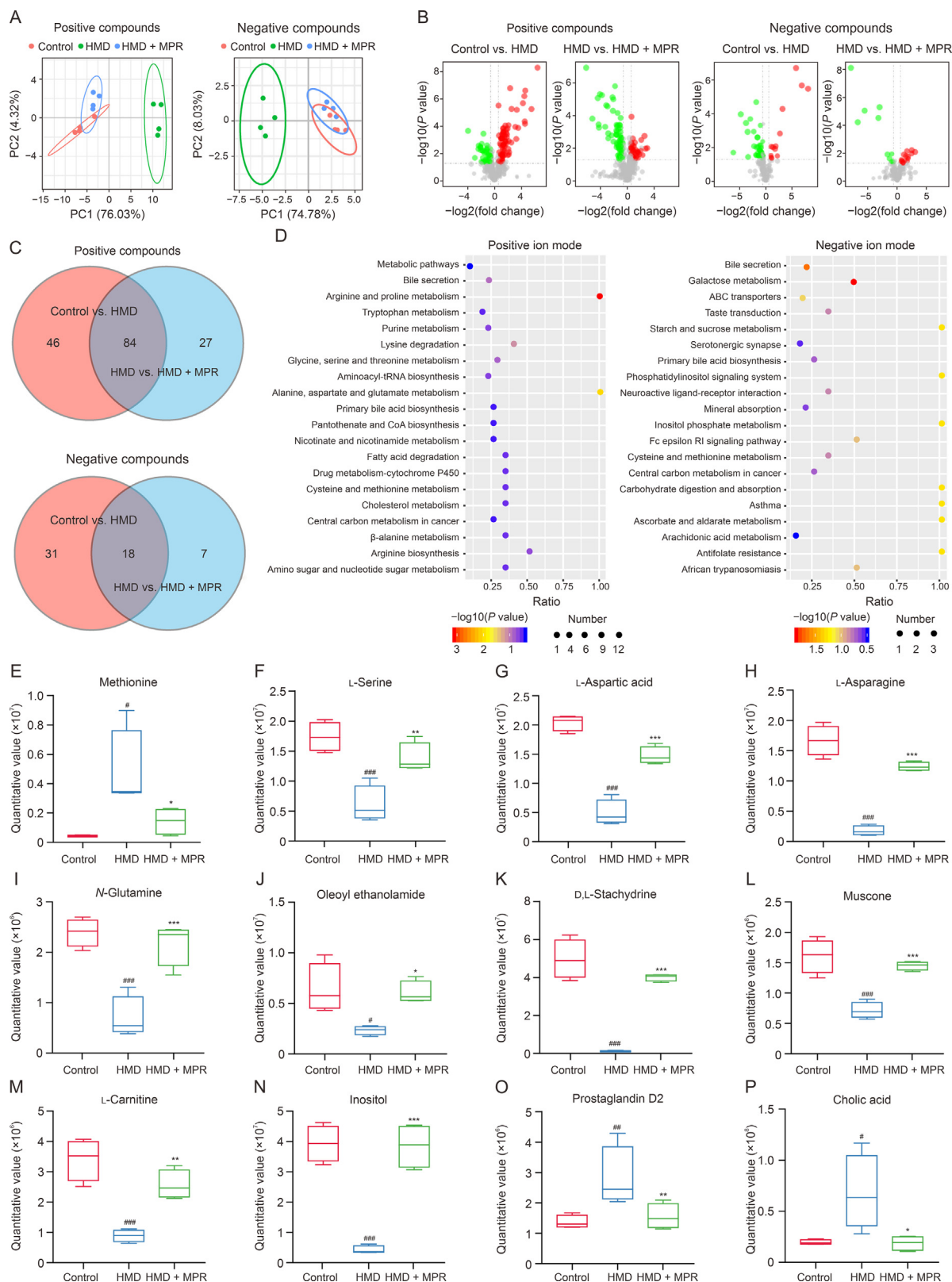
Fig. 8. Macrophage membrane (Møm)-coated rosuvastatin (RVS)-loaded Prussian blue (PB) nanoparticles (MPR NPs) ameliorates the disorder of metabolite levels caused by high methionine diet (HMD). (A) Principal component analysis (PCA) of the control, HMD, and MPR groups in positive compounds and negative compounds modes. (B) Volcano plot analysis of differential metabolites between the control vs. HMD groups and HMD vs. HMD + MPR groups under positive compounds and negative compounds. Red and green represent upregulated and down-regulated metabolites, respectively. (C) Venn gram shows co-expression metabolites between the control vs. HMD and HMD vs. HMD + MPR groups in both positive compounds and negative compounds. (D) Kyoto Encyclopedia of Genes and Genomes (KEGG) pathway involved in differential metabolites between the control, HMD, and MPR groups under positive iron mode and negative iron mode. (E–P) Box chart shows the methionine (E), l-serine (F), l-aspartic acid (G), l-asparagine (H), N-glutamine (I), oleoyl ethanolamide (J), d,l-stachydrine (K), muscone (L), l-carnitine (M), inositol (N), prostaglandin D2 (O), and cholic acid (P) quantitative values in the control, HMD, and HMD + MPR groups. Data are means ± standard deviation (SD) ($n = 4$). $^{\#}P < 0.05$, $^{\#\#}P < 0.01$, and $^{\#\#\#}P < 0.001$ vs. the control group; $^{*}P < 0.05$, $^{**}P < 0.01$, and $^{***}P < 0.001$ vs. the HMD. PC: principal component; tRNA: transfer RNA; ABC: adenosine triphosphate (ATP)-binding cassette transporter; Fc: fragment crystallizable; RI: receptor for immunoglobulin E.

compounds and 13/36 negative compounds in the control vs. HMD group. Similarly, in the HMD vs. MPR group, 44/67 positive compounds were upregulated/downregulated, as well as 15/10 negative compounds (Fig. 8B). Moreover, a Venn diagram demonstrated the co-expression of 84 metabolites in the positive compounds and 18 metabolites in the negative compounds between the control vs. HMD and HMD vs. MPR groups (Fig. 8C). A cluster heatmap clearly depicted the differences in co-expressed metabolites between the groups (Fig. S4). Furthermore, we evaluated the metabolites involved in 20 distinct metabolic pathways associated with the treatment of atherosclerosis by MPR NPs (Fig. 8D).

Anomalous methionine metabolism can contribute to the development of HHcy-induced atherosclerosis by upregulating Hcy levels. However, serine has the ability to produce cystathionine through the action of cystathionine β-synthetase, leading to the generation of cysteine and subsequent reduction in blood Hcy levels. Notably, after MPR NPs treatment, there was a decrease in methionine and an increase in l-serine in the cysteine and methionine metabolic pathways (Figs. 8E and F). Therefore, we hypothesized that MPR NPs could also reduce blood Hcy levels. Numerous studies have suggested that the modulation of pyroptosis-mediated inflammatory homeostasis and lipid metabolism is of great therapeutic interest in atherosclerosis [38]. Deficiencies in aspartic acid, asparagine, and oleyl ethanolamine have been reported to predispose the body to oxidative stress by causing glutamine metabolism disorders [39,40]. Prostaglandin D2 can induce high expression of IL-18 [41], while muscone and stachydrine can regulate the NF-κB signaling pathway and reduce the levels of inflammatory factors [42,43]. Additionally, elevated cholic acid can lead to cholestasis and inhibit cholesterol metabolism [44]. On the contrary, carnitine supplementation has been shown to decrease cholesterol levels [45]. Inositol is an essential vitamin for lipid metabolism in the body and can reduce blood lipid levels [46]. In the present study, we observed that treatment with MPR NPs resulted in increased levels of l-aspartic acid, l-asparagine, *N*-glutamine, oleyl ethanolamine, d,l-stachydrine, muscone, l-carnitine, and inositol (Figs. 8G–N), while levels of prostaglandin D2 and cholic acid were reduced (Figs. 8O and P). These changes in metabolite levels provide insights into the mechanism by which MPR NPs lower blood Hcy levels. Moreover, MPR NPs treatment led to a decrease in HHcy-induced atherosclerosis-related metabolites associated with oxidative stress, inflammation, and lipid metabolism, which are closely linked to pyroptosis.

3.7. Changes in gut microbiota after MPR NPs treatment

Recent research has reported the significant impact of changes in the composition and dysfunction of the intestinal flora on the occurrence and development of atherosclerosis [47]. Microbes present in the gut have the ability to enter the bloodstream by increasing the permeability of intestinal epithelial cells. In this study, we investigated the effect of MPR NPs on the permeability of Caco-2 cells treated with Hcy. Our findings revealed that MPR NPs effectively alleviated the reduction in levels of tight junction proteins ZO-1 and occludin caused by Hcy (Fig. S5). Given that MPR NPs may enter the intestinal system through the bloodstream and improve the intestinal microenvironment, we then performed 16S rDNA sequencing to explore the impact of MPR NPs on the gut microbiota of *ApoE*$^{-/-}$ mice. The Simpson and Shannon indexes were used to assess species richness and evenness, respectively, and demonstrated high values in all groups (Figs. 9A and B). Principal coordinate analysis (PCoA) was conducted to analyze the overall structure of the gut microbiota in mice with different treatments. The first and second principal components contributed variance values of 44.39% and 14.23%, respectively. Additionally, Fig. 9C clearly illustrates the effective differentiation of sample

clustering between the control group and the HMD group as well as the HMD group and the MPR group, with minor differences observed between the control group and the MPR group. These findings were consistent with the non-metric multidimensional scaling (NMDS) plot, which demonstrated a stress coefficient analysis value of 0.028, considered highly representative (Fig. 9D). Furthermore, the Venn diagram revealed the co-existence of 407 gut microbiota among the three groups (Fig. 9E).

The human gut microbiota is primarily composed of two dominant phyla, *Firmicutes* and *Bacteroidetes*, as well as subdominant phyla, including *Proteobacteria* and *Verrucomicrobia*. Clinical studies have observed an imbalance in the intestinal flora of patients with heart disease, predominantly characterized by an increase in the *Firmicutes*/*Bacteroidetes* ratio [48]. Additionally, *Bacteroides* has been positively associated with carotid plaque [49]. Furthermore, *Akkermansia* has been found to play a "probiotic" role in atherosclerosis by reducing total cholesterol levels and improving liver function [50]. The decreased abundance of both *Akkermansia* and *Bacteroidetes* has been linked to inflammation and the promotion of atherosclerosis progression [51]. In our study, a column plot of relative abundances was generated to observe the fraction of species with higher relative abundances at the phylum level. *Firmicutes*, *Bacteroidetes*, *Verrucomicrobia*, and *Proteobacteria* were identified as the dominant bacteria among the three groups (Fig. 9F). Treatment with MPR NPs significantly reduced the *Firmicutes*/*Bacteroidetes* ratio, while the HMD group showed an increase/decrease in *Verrucomicrobia* and *Proteobacteria* abundances. The ternary phase diagram further illustrated the enrichment of genera from *Firmicutes* and *Proteobacteria* in the HMD group and the enrichment of genera from *Bacteroidetes* and *Verrucomicrobia* in the control and MPR groups (Fig. 9G). Species abundance analysis revealed the presence of *Muribaculaceae*, *Bacteroides*, *Muribaculum* (belonging to the phylum *Bacteroidetes*), *Ileibacterium*, *Ruminococcus*, *Alloprevotella* (belonging to the phylum *Firmicutes*), and *Akkermansia* (belonging to the phylum *Verrucomicrobia*) among the top 10 microorganisms in the genus-level evolutionary tree of species (Figs. 9H and I). Similarly, the ternary phase diagram demonstrated enrichment of *Bacteroidetes* and *Verrucomicrobia* following MPR treatment, while *Firmicutes* was significantly enriched in the HMD group (Fig. 9J). Furthermore, linear discriminant analysis (LDA) and linear discriminant analysis effect size (LEfSe) analysis of taxonomic alterations confirmed the dominant set of microbes affected by HHcy and MPR NPs treatment, including p_*Verrucomicrobiota*, p_*Bacteroidota*, p_*Firmicutes*, p_*Proteobacteria*, and downstream branch gut microbiota (Figs. 9K and L and Table S1).

The results of this study suggest that the administration of MPR NPs can improve the gut microbiota microenvironment in HMD-induced *ApoE*$^{-/-}$ mice. Specifically, it increases the abundance of beneficial bacteria while reducing the levels of pro-inflammatory and pro-atherosclerosis microorganisms. These findings provide a theoretical foundation for exploring the relationship between gut microbiota and nano-drugs in the treatment of HHcy-induced atherosclerosis. In conclusion, the treatment with MPR NPs shows potential in ameliorating the disorder of gut microbiota induced by HMD in *ApoE*$^{-/-}$ mice. This is achieved through the modulation of bacterial compositions, increasing the presence of beneficial bacteria and reducing the levels of pro-inflammatory and pro-atherosclerosis microorganisms. The significance of these results lies in the understanding of the gut microbiota-nano-drug interaction and its potential application in treating HHcy-induced atherosclerosis.

3.8. Safety and biocompatibility assessment of MPR NPs

Low cytotoxicity and excellent blood compatibility are crucial indicators of the safety of nano-drugs. To assess the potential for
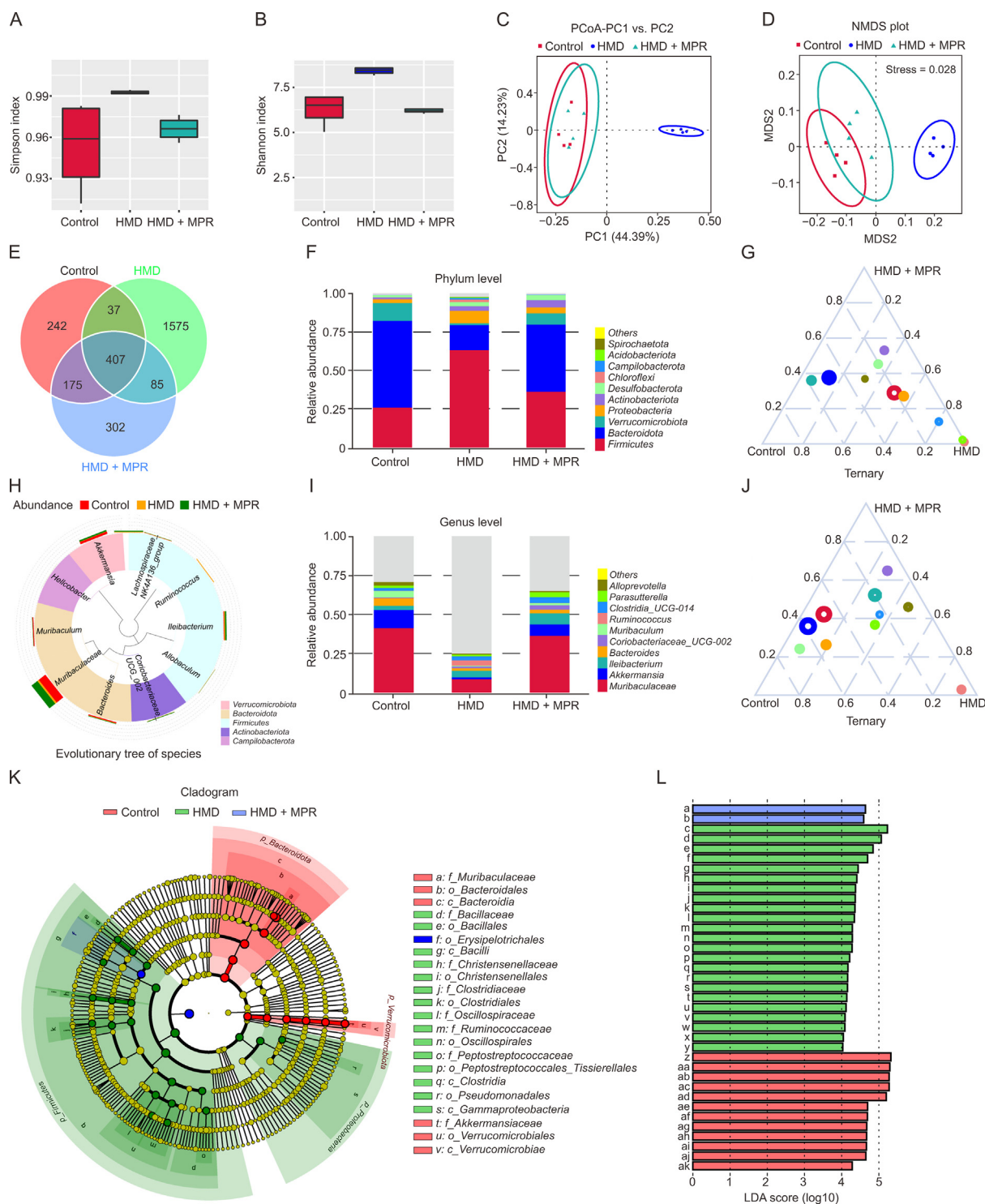
Fig. 9. Macrophage membrane (Møm)-coated rosuvastatin (RVS)-loaded Prussian blue (PB) nanoparticles (MPR NPs) improve the intestinal microenvironment in apolipoprotein E knockout (*ApoE$^{-/-}$*) mice fed high methionine diet (HMD). (A, B) Simpson (A) and Shannon indexes (B) for the control, HMD, and HMD + MPR groups. (C) Principal coordinate analysis (PCoA) plots show the differences between the control, HMD, and HMD + MPR groups. (D) The non-metric multidimensional scaling (NMDS) plot for reflecting the ordering relationship of the values in the distance matrix. (E) Venn diagram showing the co-existing gut microbiota among the control, HMD, and HMD + MPR groups. (F) The columns plot species abundance at the microbial phylum level among the control, HMD, and HMD + MPR groups. (G) Ternary phase diagram of genera from the top 10 most abundant phylum among the control, HMD, and HMD + MPR groups. (H) Evolutionary tree of genus level in the control, HMD, and HMD + MPR groups. (I) The columns plot species abundance at the microbial genus level among the control, HMD, and HMD + MPR groups. (J) Ternary phase diagram of genera from the top 10 most abundant genus among the control, HMD, and HMD + MPR groups. (K, L) Linear discriminant analysis (LDA) scores (K) from linear discriminant analysis effect size (LEfSe) analyses (L) were analyzed for taxa with the highest differential abundance and among the control, HMD, and HMD + MPR groups (*n* = 4). Detailed meanings of all code names in Fig. 9L are shown in Table S1. PC: principal component; MDS2: multidimensional scaling 2.

hemolysis and clotting, we added various concentrations of MPR NPs to the blood solution. Surprisingly, even at a concentration of 30 μg/mL (Figs. S6A and B), we observed minimal instances of hemolysis and clotting. Additionally, the morphology of red blood cells remained largely unchanged after 6 h of incubation with MPR NPs (Fig. S6C). Furthermore, we performed a CCK-8 assay to evaluate the effect of MPR NPs on the viability of different cell lines, including RAW264.7 cells, HUVECs, VSMCs, and HL7702 cells. Interestingly, we found that 10 μg/mL of MPR NPs had no significant effect on the viability of these cell lines. However, at a concentration of 30 μg/mL, MPR NPs exhibited cytotoxicity towards RAW264.7 cells and HUVECs. Importantly, the viability of HL7702 cells was only slightly affected at concentrations above 20 and 30 μg/mL (Fig. S6D). Considering the fact that the working concentration of MPR NPs was lower than 20 μg/mL, these results indicate that MPR NPs can be used for *in vivo* applications with acceptable biosafety. In conclusion, the results of our study confirm the low cytotoxicity and excellent blood compatibility of MPR NPs. These findings contribute to the overall safety profile of MPR NPs and support their potential use in *in vivo* applications.

Serum biochemical tests and pathological studies were performed to investigate the *in vivo* effects of MPR NPs further. As shown in Figs. S7A and B, levels of aspartate transaminase (AST) and alanine aminotransferase (ALT) were higher in the HMD group compared to the control group. Additionally, H&E staining revealed vacuolated changes (indicated by the arrows) in the liver of the HMD group (Fig. S7C), indicating abnormal liver function due to fatty infiltration. However, these phenomena were significantly alleviated in the MPR groups. It is worth noting that the RVS group exhibited a more significant increase in AST and ALT levels (Figs. S7A and B). Furthermore, we observed certain pathological changes in the liver sections of mice in the RVS group. These changes were characterized by the deeply stained nucleus, lightly stained diffuse cytoplasm, and the presence of some multinucleated cells, indicating mild cellular edema and functional changes (Fig. S7C), possibly due to the long-term high-dose RVS administration. However, MPR NPs show no significant impact on blood routine analysis (Figs. S8A−D) and do not induce observable abnormalities in the liver (Fig. S7C). These results suggest that MPR NPs can attenuate the side effects associated with long-term RVS use. In summary, MPR NPs can alleviate abnormal liver function caused by fatty infiltration, as indicated by the decrease in AST and ALT levels. These findings highlight the potential of MPR NPs as a safer alternative to long-term RVS administration. Moreover, irregularly shaped dark granular substances were observed in the liver of the PB group (Fig. S7C). Based on the results of organ distribution (Figs. 3E and F), we speculate that these substances are unmetabolized PB NPs. Therefore, while PB NPs did not cause liver damage, they may not accurately localize to atherosclerotic lesions due to the lack of Møm coating. Finally, Blood routine analysis and HE staining revealed no significant abnormal changes compared to the HMD group (Fig. S8E).

4. Conclusion

In conclusion, we have successfully developed MPR NPs as a nano-drug that combines the beneficial effects of RVS, such as its anti-inflammatory and lipid-lowering properties, while overcoming its toxic side effects. The incorporation of Møm coating enhances the biological characteristics of MPR NPs, resulting in an extended $t_{1/2}$ and improved targeting capabilities, specifically for atherosclerotic lesions. Through the regulation of TLR4/HIF-1α/ NLRP3 pathways, MPR NPs effectively mitigate Hcy-induced macrophage pyroptosis. The *in vivo* studies have further demonstrated the high therapeutic efficacy and safety of MPR NPs,

highlighting their potential as a promising treatment option. Furthermore, the metabolomics and 16S rDNA sequencing analyses have revealed that MPR NPs can positively modulate the metabolic pathways and resolve metabolite abnormalities induced by HHcy. Additionally, they also address the gut microbiota disorder caused by HMD in *ApoE⁻/⁻* mice. Taken together, the remarkable features of MPR NPs, including their improved safety profile, targeted delivery to atherosclerotic lesions, retained therapeutic effects, and modulation of metabolic pathways and gut microbiota, make them a promising therapeutic strategy for HHcy-induced atherosclerosis. Overall, MPR NPs represent a novel nano-drug that offers a potential solution for the treatment of HHcy-induced atherosclerosis, providing improved therapeutic outcomes.

CRediT author statement

Dayue Liu and **Anning Yang:** Conceptualization, Data curation, Methodology, Formal analysis, Validation, Project Administration, Writing - Original draft preparation; **Yulin Li**, **Zhenxian Li**, **Peidong You**, and **Hongwen Zhang:** Methodology, Validation, Project Administration; **Shangkun Quan**, **Yue Sun**, and **Yaling Zeng:** Validation; **Shengchao Ma**, **Jiantuan Xiong**, **Yinju Hao**, and **Guizhong Li:** Resources, Funding acquisition; **Bin Liu**, **Huiping Zhang**, and **Yideng Jiang:** Funding acquisition, Resources, Supervision, Writing - Reviewing and Editing.

Declaration of competing interest

The authors declare that there are no conflicts of interest.

Acknowledgments

Appendix A. Supplementary data

Supplementary data to this article can be found online at https://doi.org/10.1016/j.jpha.2024.01.005.

References

[1] N. Zhang, L. Zhu, X. Wu, et al., The regulation of Ero1-alpha in homocysteine-induced macrophage apoptosis and vulnerable plaque formation in atherosclerosis, Atherosclerosis 334 (2021) 39−47.

[2] X. Lu, Impact of macrophages in atherosclerosis, Curr. Med. Chem. 23 (2016) 1926−1937.

[3] J. Shah, V. Lingiah, N. Pyrsopoulos, et al., Acute liver injury in a patient treated with rosuvastatin: A rare adverse effect, Gastroenterology Res. 12 (2019) 263−266.

[4] M. Cheraghi, B. Negahdari, H. Daraee, et al., Heart targeted nanoliposomal/ nanoparticles drug delivery: An updated review, Biomed. Pharmacother. 86 (2017) 316−323.

[5] Z. Qin, Y. Li, N. Gu, Progress in applications of Prussian blue nanoparticles in biomedicine, Adv. Healthc. Mater. 7 (2018), e1800347.

[6] Y. Zhang, Y. Yin, W. Zhang, et al., Reactive oxygen species scavenging and inflammation mitigation enabled by biomimetic Prussian blue analogues boycott atherosclerosis, J. Nanobiotechnology 19 (2021), 161.

[7] J. Lopes, D. Lopes, M. Pereira-Silva, et al., Macrophage cell membrane-cloaked nanoplatforms for biomedical applications, Small Methods 6 (2022), e2200289.

[8] R. Wang, Y. Wang, N. Mu, et al., Activation of NLRP3 inflammasomes contributes to hyperhomocysteinemia-aggravated inflammation and atherosclerosis in *ApoE*-deficient mice, Lab Invest. 97 (2017) 922−934.

[9] J. Shi, Y. Zhao, K. Wang, et al., Cleavage of GSDMD by inflammatory caspases determines pyroptotic cell death, Nature 526 (2015) 660−665.

[10] P. Yu, X. Zhang, N. Liu, et al., Pyroptosis: mechanisms and diseases, Signal Transduct. Target. Ther. 6 (2021), 128.

[11] S. Ma, Y. Hao, Y. Jiao, et al., Homocysteine-induced oxidative stress through TLR4/NF-κB/DNMT1-mediated LOX-1 DNA methylation in endothelial cells, Mol. Med. Rep. 16 (2017) 9181−9188.

[12] M. Xu, Z. Ye, X. Zhao, et al., Deficiency of tenascin-C attenuated cardiac injury by inactivating TLR4/NLRP3/caspase-1 pathway after myocardial infarction, Cell. Signal. 86 (2021), 110084.

[13] Z. Hong, X. Zhang, T. Zhang, et al., The ROS/GRK2/HIF-1α/NLRP3 pathway mediates pyroptosis of fibroblast-like synoviocytes and the regulation of monomer derivatives of paeoniflorin, Oxid. Med. Cell. Longev. 2022 (2022), 4566851.

[14] R. Chen, T. Chen, Z. Zhou, et al., Integrated pyroptosis measurement and metabolomics to elucidate the effect and mechanism of tangzhiqing on atherosclerosis, Front. Physiol. 13 (2022), 937737.

[15] Y. Yang, Y. Zhang, Y. Xu, et al., Dietary methionine restriction improves the gut microbiota and reduces intestinal permeability and inflammation in high-fat-fed mice, Food Funct. 10 (2019) 5952−5968.

[16] Q. Chen, C. Wang, F. Zhao, et al., Effects of methionine partially replaced by methionyl-methionine dipeptide on intestinal function in methionine-deficient pregnant mice, J. Anim. Physiol. Anim. Nutr. 103 (2019) 1610−1618.

[17] M. Witkowski, T.L. Weeks, S.L. Hazen, Gut microbiota and cardiovascular disease, Circ. Res. 127 (2020) 553−570.

[18] X. Liang, H. Li, X. Li, et al., Highly sensitive H₂O₂-scavenging nano-bionic system for precise treatment of atherosclerosis, Acta Pharm. Sin. B 13 (2023) 372−389.

[19] X. Zhang, Y. Qin, X. Wan, et al., Rosuvastatin exerts anti-atherosclerotic effects by improving macrophage-related foam cell formation and polarization conversion via mediating autophagic activities, J. Transl. Med. 19 (2021), 62.

[20] J.D. Nickels, K.S. Bonifer, R.R. Tindall, et al., Improved chemical and isotopic labeling of biomembranes in *Bacillus subtilis* by leveraging CRISPRi inhibition of beta-ketoacyl-ACP synthase (*fabF*), Front. Mol. Biosci. 9 (2022), 1011981.

[21] X. Hou, H. Zeng, X. Chi, et al., Pathogen receptor membrane-coating facet structures boost nanomaterial immune escape and antibacterial performance, Nano Lett. 21 (2021) 9966−9975.

[22] J.W. Calderwood, J.M. Williams, M.D. Morgan, et al., ANCA induces beta2 integrin and CXC chemokine-dependent neutrophil-endothelial cell interactions that mimic those of highly cytokine-activated endothelium, J Leukoc. Biol 77 (2005) 33−43.

[23] X. Chen, Q. Wang, L. Liu, et al., Double-sided effect of tumor microenvironment on platelets targeting nanoparticles, Biomaterials 183 (2018) 258−267.

[24] N. Khatoon, Z. Zhang, C. Zhou, et al., Macrophage membrane coated nanoparticles: A biomimetic approach for enhanced and targeted delivery, Biomater. Sci. 10 (2022) 1193−1208.

[25] M.F. Linton, V.R. Babaev, J. Huang, et al., Macrophage apoptosis and efferocytosis in the pathogenesis of atherosclerosis, Circ. J. 80 (2016) 2259−2268.

[26] M. Lombardi, M.E. Mantione, D. Baccellieri, et al., P2X7 receptor antagonism modulates IL-1β and MMP9 in human atherosclerotic vessels, Sci. Rep. 7 (2017), 4872.

[27] J. Geng, H. Xu, W. Fu, et al., Rosuvastatin protects against endothelial cell apoptosis *in vitro* and alleviates atherosclerosis in *ApoE⁻/⁻* mice by suppressing endoplasmic reticulum stress, Exp. Ther. Med. 20 (2020) 550−560.

[28] S. Liu, J. Tao, F. Duan, et al., HHcy induces pyroptosis and atherosclerosis via the lipid raft-mediated NOX-ROS-NLRP3 inflammasome pathway in *ApoE⁻/⁻* mice, Cells 11 (2022), 2438.

[29] J. Yang, L. Wise, K.I. Fukuchi, TLR4 cross-talk with NLRP3 inflammasome and complement signaling pathways in Alzheimer's disease, Front. Immunol. 11 (2020), 724.

[30] A. Ajoolabady, Y. Bi, D.J. McClements, et al., Melatonin-based therapeutics for atherosclerotic lesions and beyond: Focusing on macrophage mitophagy, Pharmacol. Res. 176 (2022), 106072.

[31] Y.-W. Wang, H.-Z. Dong, Y.-X. Tan, et al., HIF-1α-regulated lncRNA-TUG1 promotes mitochondrial dysfunction and pyroptosis by directly binding to FUS in myocardial infarction, Cell Death Discov 8 (2022), 178.

[32] X. Ma, J. Hao, J. Wu, et al., Prussian blue nanozyme as a pyroptosis inhibitor alleviates neurodegeneration, Adv. Mater. 34 (2022), e2106723.

[33] C. Xiao, C. Tong, J. Fan, et al., Biomimetic nanoparticles loading with gamabutolin-indomethacin for chemo/photothermal therapy of cervical cancer and anti-inflammation, J. Control. Release 339 (2021) 259−273.

[34] A. Chen, Z. Chen, Y. Zhou, et al., Rosuvastatin protects against coronary microembolization-induced cardiac injury via inhibiting NLRP3 inflammasome activation, Cell Death Dis. 12 (2021), 78.

[35] C. Thomas, D. Leleu, D. Masson, Cholesterol and HIF-1α: Dangerous liaisons in atherosclerosis, Front. Immunol. 13 (2022), 868958.

[36] I. Hussain, S. Waheed, K.A. Ahmad, et al., *Scutellaria baicalensis* targets the hypoxia-inducible factor-1α and enhances cisplatin efficacy in ovarian cancer, J. Cell. Biochem. 119 (2018) 7515−7524.

[37] L. Shen, H. Li, W. Chen, et al., Integrated application of transcriptome and metabolomics reveals potential therapeutic targets for the polarization of atherosclerotic macrophages, Biochim. Biophys. Acta Mol. Basis Dis. 1868 (2022), 166550.

[38] L. Anto, C.N. Blesso, Interplay between diet, the gut microbiome, and atherosclerosis: Role of dysbiosis and microbial metabolites on inflammation and disordered lipid metabolism, J. Nutr. Biochem. 105 (2022), 108991.

[39] H. Jian, Q. Xu, X. Wang, et al., Amino acid and fatty acid metabolism disorders trigger oxidative stress and inflammatory response in excessive dietary valine-induced NAFLD of laying hens, Front. Nutr. 9 (2022), 849767.

[40] R. Cazzola, M. Rondanelli, *N*-oleoyl-phosphatidyl-ethanolamine and epigallo catechin-3-gallate mitigate oxidative stress in overweight and class I obese people on a low-calorie diet, J. Med. Food 23 (2020) 319−325.

[41] H.S. Lee, S.J. Yun, J.M. Ha, et al., Prostaglandin D₂ stimulates phenotypic changes in vascular smooth muscle cells, Exp. Mol. Med. 51 (2019) 1−10.

[42] H. Wu, M. Zhang, W. Li, et al., Stachydrine attenuates IL-1β-induced inflammatory response in osteoarthritis chondrocytes through the NF-κB signaling pathway, Chem. Biol. Interact. 326 (2020), 109136.

[43] Y. Du, X. Gu, H. Meng, et al., Muscone improves cardiac function in mice after myocardial infarction by alleviating cardiac macrophage-mediated chronic inflammation through inhibition of NF-κB and NLRP3 inflammasome, Am. J. Transl. Res. 10 (2018) 4235−4246.

[44] X. Gao, Y. Ruan, X. Zhu, et al., Deoxycholic acid promotes pyroptosis in free fatty acid-induced steatotic hepatocytes by inhibiting PINK1-mediated mitophagy, Inflammation 45 (2022) 639−650.

[45] M.M. Sayed-Ahmed, M.M. Khattab, M.Z. Gad, et al., L-carnitine prevents the progression of atherosclerotic lesions in hypercholesterolaemic rabbits, Pharmacol. Res. 44 (2001) 235−242.

[46] R. Tabrizi, V. Ostadmohammadi, K.B. Lankarani, et al., The effects of inositol supplementation on lipid profiles among patients with metabolic diseases: a systematic review and meta-analysis of randomized controlled trials, Lipids Health Dis. 17 (2018), 123.

[47] K. Sachin, S.K. Karn, Microbial fabricated nanosystems: Applications in drug delivery and targeting, Front. Chem. 9 (2021), 617353.

[48] Y. Wang, Y. Xu, X. Xu, et al., *Ginkgo biloba* extract ameliorates atherosclerosis via rebalancing gut flora and microbial metabolism, Phytother. Res. 36 (2022) 2463−2480.

[49] Z. Wang, B.A. Peters, M. Usyk, et al., Gut microbiota, plasma metabolomic profiles, and carotid artery atherosclerosis in HIV infection, Arterioscler. Thromb. Vasc. Biol. 42 (2022) 1081−1093.

[50] T. Zhang, Q. Li, L. Cheng, et al., *Akkermansia muciniphila* is a promising probiotic, Microb. Biotechnol. 12 (2019) 1109−1125.

[51] S. Sun, X. Xu, L. Liang, et al., Lactic acid-producing probiotic *Saccharomyces cerevisiae* attenuates ulcerative colitis via suppressing macrophage pyroptosis and modulating gut microbiota, Front. Immunol. 12 (2021), 777665.